

Helsinki University of Technology  
Department of Engineering Physics and Mathematics

Jussi Nurminen

**Simulation of the SSS method for a 76-channel MEG instrument**

Master's thesis submitted for partial requirements for the degree of Master  
of Science in Technology

Espoo, 1.12.2004

Supervisor: Professor Toivo Katila

Instructor: Professor Yoshio Okada, University of New Mexico

<b>Tekijä:</b>	Jussi Nurminen
<b>Työn nimi:</b>	SSS-menetelmän simulointi 76-kanavaiselle MEG-laitteelle
<b>English title:</b>	Simulation of the SSS method for a 76-channel MEG instrument
<b>Päivämäärä:</b>	1.12.2004
<b>Sivumäärä:</b>	51
<b>Osasto:</b>	Teknillisen fysiikan ja matematiikan osasto
<b>Professori:</b>	Tfy-99 Biofysiikka ja lääketieteellinen tekniikka
<b>Työn valvoja:</b>	Professori Toivo Katila
<b>Työn ohjaaja:</b>	Professori Yoshio Okada, University of New Mexico
<p>babySQUID<sup>TM</sup> on uusi vauvatutkimuksiin suunniteltu 76-kanavainen magnetoenkefalografia (MEG) -laite. Sen on tarkoitus toimia ilman magneettista suojausta, joten laitteen käyttö edellyttää tehokkaita häiriönpoistomenetelmiä. Eräs lupaava uusi menetelmä on Signal Space Separation (SSS). Sillä voidaan rekonstruoida MEG-laitteen anturiston lähellä olevien signaalilähteiden kentät ja poistaa kauempana olevien häiriölähteiden aiheuttamat kentät minimaalisin oletuksin. Tässä diplomityössä tutkittiin SSS-menetelmän toimintaa babySQUID-laitteella tietokonesimulaatiota käyttäen.</p> <p>Koska babySQUID-laitteessa käytetään vain yhtä sensortyyppiä (aksiaalinen gradiometri), SSS-matriisista tulee hyvin häiriöaltis. Työssä löydettiin tämän ongelman ratkaisuun sopiva regularisointimenetelmä PP-TSVD (piecewise polynomial truncated singular value decomposition). Menetelmää käyttäen on mahdollista saada stabiileja ja tarkkoja SSS-ratkaisuja. Esim. anturistosta 5 m päässä olevan häiriölähteen kenttä voidaan poistaa, vaikka sen voimakkuus on 10-kertainen signaalilähteen kenttään verrattuna.</p> <p>Laitteen verrattain vähäinen kanavamäärä rajoittaa käytettävissä olevien kantavektorien määrää. Tästä huolimatta 8 mm päässä anturistosta olevan signaalilähteen rekonstruointi onnistuu. Kyky poistaa häiriölähteiden kenttiä huononee tosin nopeasti kun niitä tuodaan alle 1 m päähän anturistosta, ja signaalien rekonstruointi onnistuu parhaiten kun signaalilähteet on rajattu tiettyyn osaan anturistoa.</p> <p>Simulaatiot osoittavat että SSS-menetelmä on varsin herkkä gradiometrien epätasapainolle, joka saattaa babySQUID-laitteessa olla niin suuri että ratkaisut häiriintyvät merkittävästi. Tässä työssä käytettiin vain simuloitua dataa, ja menetelmän lopullinen testaus tulee vaatimaan oikean mittausdatan käyttöä.</p>	
<b>Avainsanat:</b>	magnetoenkefalografia, MEG, Signal Space Separation, SSS
<b>Ei lainata ennen:</b>	<b>Työn sijaintipaikka:</b>

<b>Author:</b>	Jussi Nurminen
<b>Title:</b>	Simulation of the SSS method for a 76-channel MEG instrument
<b>Finnish title:</b>	SSS-menetelmän simulointi 76-kanavaiselle MEG-laitteelle
<b>Date:</b>	1.12.2004
<b>Pages:</b>	51
<b>Department:</b>	Department of Engineering Physics and Mathematics
<b>Chair:</b>	Tfy-99 Biophysics and Biomedical Engineering
<b>Supervisor:</b>	Professor Toivo Katila
<b>Instructor:</b>	Professor Yoshio Okada, University of New Mexico
<p>The babySQUID<sup>TM</sup> is a new 76-channel magnetoencephalography (MEG) instrument designed for infant studies. The goal of the design is to be able to operate in a magnetically unshielded environment, which means that powerful noise cancellation methods are needed. A promising new method is Signal Space Separation (SSS). Using only minimal assumptions, it is able to reconstruct fields of signal sources that are close to the sensor array while rejecting fields of disturbance sources located farther away. In this work, the SSS method was evaluated for the babySQUID instrument using a computer simulation.</p> <p>Because the babySQUID employs just one type of magnetic field sensor (axial gradiometer), the SSS matrix becomes severely ill-conditioned. It was found that a regularization method called PP-TSVD (piecewise polynomial truncated singular value decomposition) is well suited for dealing with this problem. Using this method, it is possible to get stable and accurate SSS solutions. For example, the field of a disturbance source 5 m away from the sensor array can be cancelled even when it is 10 times as strong as the field of the signal source.</p> <p>The relatively low number of channels in the babySQUID limits the number of SSS basis vectors that can be used. Despite this limitation, signal sources as close as 8 mm to the sensor array can be reconstructed. However, the ability to reject fields of disturbance sources gets rapidly worse when they are moved closer than 1 m to the sensor array, and reconstruction of signals works best when the signal sources are confined to a certain region on the sensor array.</p> <p>As shown by the simulations, the SSS method is sensitive to gradiometer imbalance, and the imbalance of the babySQUID sensors may be large enough to seriously disturb the solutions. This work used only simulated data, and the final testing of the method will require real measurement data.</p>	
<b>Keywords:</b>	magnetoencephalography, MEG, Signal Space Separation, SSS
<b>Not borrowable until:</b>	<b>Library code:</b>

# Preface

This work was done in Dr. Yoshio Okada's MEG laboratory in Albuquerque, New Mexico. I wish to thank Dr. Okada for giving me the opportunity to visit the US and work on a project involving a new MEG instrument.

Several other people deserve my thanks. Samu Taulu originally came up with the idea of simulating the SSS method, and his help was very valuable during the project. The Tristan guys worked hard to make the babySQUID a reality; special thanks to Kevin Pratt and Christopher Atwood. My colleagues Shingo Murakami, Tongsheng Zhang and Yaozhi Wang were very helpful and made my life in Albuquerque easier.

I am also grateful to my family and friends for their support.

No animals were harmed during the production of this thesis, except for a few fish used for sushi on special occasions. The harm done to human beings (including the author) was kept within reasonable limits.

# List of abbreviations

DC	Direct current
EEG	Electroencephalography
fMRI	Functional magnetic resonance imaging
MEG	Magnetoencephalography
MTSVD	Modified truncated singular value decomposition
NRMS	Normalized root mean square
PET	Positron emission tomography
PP-TSVD	Piecewise polynomial truncated singular value decomposition
SQUID	Superconducting quantum interference device
SSS	Signal Space Separation
SVD	Singular value decomposition
TSVD	Truncated singular value decomposition

# Contents

<b>1</b>	<b>Introduction</b>	<b>1</b>
<b>2</b>	<b>MEG and the babySQUID</b>	<b>3</b>
2.1	Measurement technology . . . . .	4
2.2	The babySQUID . . . . .	6
2.2.1	Sensor layout . . . . .	7
2.2.2	The gradiometers . . . . .	7
2.2.3	Noise cancellation . . . . .	9
<b>3</b>	<b>Methods</b>	<b>10</b>
3.1	The forward problem . . . . .	10
3.2	The SSS method . . . . .	12
3.3	Regularization . . . . .	16
3.3.1	The pseudoinverse and SVD . . . . .	16
3.3.2	Tikhonov regularization . . . . .	18
3.3.3	TSVD . . . . .	18
3.3.4	MTSVD . . . . .	19
3.3.5	PP-TSVD . . . . .	20
3.4	Implementation of the simulation . . . . .	20
3.4.1	Integration of the magnetic fields . . . . .	21

3.4.2	Regularization . . . . .	21
3.4.3	Simulated sensor noise . . . . .	22
<b>4</b>	<b>Results</b>	<b>23</b>
4.1	Preliminary issues . . . . .	23
4.2	Regularization . . . . .	26
4.2.1	Reconstruction speed . . . . .	29
4.2.2	Limitations imposed by the SSS geometry . . . . .	29
4.3	Evaluations of the regularized SSS method . . . . .	29
4.3.1	External sources at different distances . . . . .	29
4.3.2	Sources in the intermediate space . . . . .	34
4.3.3	Filtering a time-dependent signal . . . . .	36
4.4	Effect of nonideal properties of the sensor array . . . . .	37
4.4.1	Errors in sensor geometry data . . . . .	37
4.4.2	Gradiometer imbalance . . . . .	38
4.4.3	Calibration errors . . . . .	39
<b>5</b>	<b>Discussion</b>	<b>41</b>
<b>A</b>	<b>The Laplace equation and spherical harmonics</b>	<b>44</b>
A.1	Solving the Laplace equation . . . . .	44
A.2	Gradients of basic solutions . . . . .	47
A.3	Associated Legendre polynomials . . . . .	48

# Chapter 1

## Introduction

Magnetoencephalography (MEG) [6, 3] is a noninvasive way to study the functioning of the human brain, closely related to electroencephalography (EEG). It is based on measuring the weak magnetic fields generated by neuronal currents. The main advantages of MEG are excellent time resolution (compared to other imaging methods such as fMRI and PET) and easier source localization compared to EEG. However, MEG requires expensive, sophisticated instrumentation and usually a special magnetically shielded room.

MEG has been used to study human adults since the 1970s. An emerging area of research is the application of MEG to infant studies, which offers new possibilities for studying the development of the brain. This area also presents some novel technical challenges, in part because the existing MEG hardware is designed for adult use. To realize the full potential of MEG in infant studies, it is necessary to develop new instruments specifically for this purpose.

The babySQUID<sup>TM</sup> is a new MEG instrument developed for infant studies. The goal of the babySQUID design is not only to create an instrument well suited to infant studies, but also to make it work in unshielded environments. This requires application of various signal processing techniques for noise reduction. Recently, an elegant noise cancellation technique for MEG has been developed by Taulu et al. [14]. The method is called Signal Space Separation (SSS), and it is based on separating the fields of the signal and disturbance sources based on their physical properties. The purpose of this work is to evaluate the SSS algorithm on the babySQUID using a computer model of the sensor array.

The organization of the thesis is as follows. Chapter 2 contains a short intro-

duction to MEG and a description of the babySQUID instrument. Chapter 3 introduces the SSS method and some regularization techniques. Results of the SSS simulations are presented in Chapter 4. Discussion and conclusions follow in Chapter 5.

### **Contribution of the author**

The simulation programs used in the thesis were all written by the author in the Matlab environment. The author designed the simulation experiments, with suggestions from Samu Taulu and Yoshio Okada. For the regularization, routines from Regularization Toolbox by Per Christian Hansen [8] were used.

## Chapter 2

# MEG and the babySQUID

The communication of neurons in the human brain involves electrical currents. These currents give rise to electromagnetic fields outside the head. This makes it possible to obtain useful information about the functioning of the brain without making invasive measurements (such as inserting needle electrodes into the brain tissue).

Measurements of the electric potential on the scalp are called electroencephalography (EEG). The first measured human EEGs were reported in 1929 [2]. Magnetoencephalography, which refers to measurement of the magnetic fields produced by the neural currents, is technically much more difficult. The reason is that the fields are very weak and easily masked by environmental magnetic disturbances. David Cohen made the first MEG measurements in 1968 using induction coils [3]. A few years later, he carried out the first measurements using SQUID (Superconducting Quantum Interference Device) sensors, which are the basis of modern MEG instruments [4]. The SQUID is an extremely sensitive magnetic field detector based on quantum effects.

Modern MEG instruments usually have tens to hundreds of sensors. This makes it possible to get a comprehensive picture of the magnetic field produced by the brain activity without moving the instrument or the head. The resulting data are analyzed, often with the intent of localizing the current sources in the brain that are responsible for producing the field. In the solution of this inverse problem, MEG has an advantage over EEG, since the magnetic fields are not markedly disturbed by the skull and scalp layers in the frequency range of interest. Therefore the precise conductivity details of the head, which are often unavailable, are not needed for MEG source analysis.

## 2.1 Measurement technology

The amplitude of the magnetic fields measured with conventional, commercial MEG instruments is typically 10 – 1000 fT. The frequencies of interest usually lie below 50 Hz, though frequencies ranging up to 1 kHz have been studied. The signals are about a billion times smaller than the earth's magnetic field, so very sensitive instruments are needed. The SQUID is in fact the most sensitive magnetic field detector known. Its purpose is to convert the weak magnetic flux to a voltage that can be measured. Here we briefly discuss the DC SQUID, which is the preferred type of SQUID in modern neuromagnetic measurements.

The DC SQUID (Fig. 2.1) is a superconducting ring interrupted by two weak links (Josephson junctions) which have a lower critical current than the main ring. The critical current is the maximum electric current that a superconductor can carry without developing resistance.

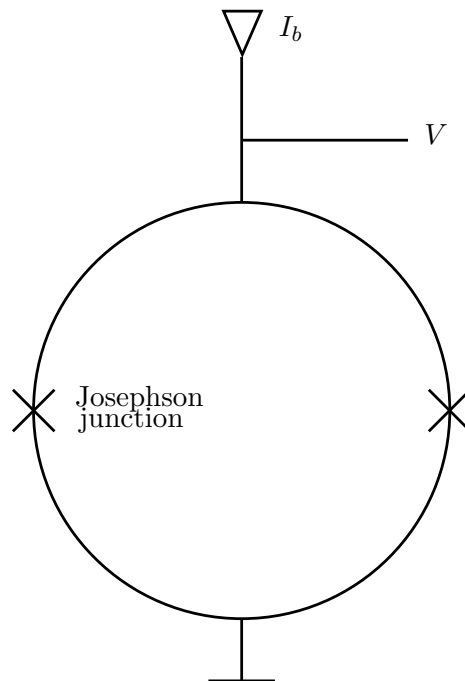


Figure 2.1: A schematic representation of the SQUID.

As in the case of a simple superconducting ring, an external flux threading the SQUID ring will give rise to a compensatory current. When a suitable bias current  $I_b$  ( $I_b \approx 2I_c$ , where  $I_c$  is the junction critical current) is injected into the ring, the junctions will be resistive for all applied flux values and

a flux-dependent voltage develops across the ring. The voltage  $V$  depends periodically on the applied flux with a period of  $\phi_0 = h/2e \approx 2.07$  fWb, where  $h$  is Planck's constant and  $e$  the electron charge.

The changes in the applied flux could be measured by counting the periods that the voltage goes through. However, in practice it is simpler to keep the SQUID at a constant operating point (constant voltage and magnetic flux) using a negative feedback loop. The output voltage of the SQUID is kept constant by applying a compensatory magnetic field with a feedback coil, and the voltage required to drive the coil is tracked instead of the SQUID output voltage.

The magnetic flux is normally brought to the SQUID by a flux transformer. The transformer pickup coil can be a simple loop (magnetometer) or a series of loops (gradiometer). Different types of gradiometers exist; a first-order axial gradiometer is illustrated in Fig. 2.2.

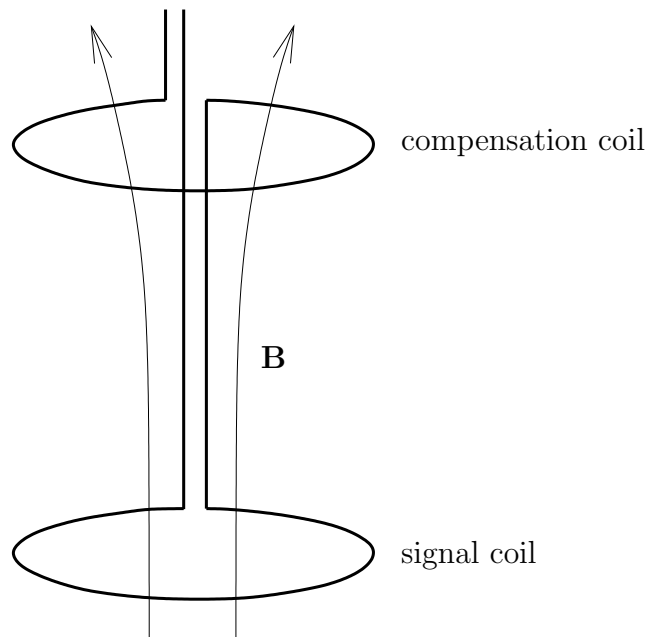


*Figure 2.2: A first-order axial gradiometer. A homogenous magnetic field  $B$  induces currents of equal magnitude in the coils, resulting in no output. A nonhomogenous field induces currents of different magnitude and causes an output.*

A gradiometer is useful, since faraway disturbance sources give rise to nearly homogenous fields. In contrast, a field caused by a source close to the gradiometer will be strongly nonhomogenous.

Both the flux transformers and the SQUIDs need to be in a superconducting state. As conventional low temperature superconductors are usually used in neuromagnetic measurements, this requires cooling them to very low temperatures (less than 10 K). Most often this is achieved by suspending the flux transformers and SQUIDs in liquid helium bath. The liquid helium is kept in a vacuum-isolated vessel called a dewar, which works like a thermos bottle.

## 2.2 The babySQUID

The babySQUID<sup>TM</sup> [10] is a 76-channel axial gradiometer instrument designed for infant studies. A computer rendering of the babySQUID cart is shown in Fig. 2.3. The baby is lying on a bed with his or her head positioned over the sensor array. The larger cart contains the dewar and the sensor array. The acquisition electronics are in the smaller cart. Attached to the larger cart is an infrared tracking camera, which is used to record the position of the baby's head.

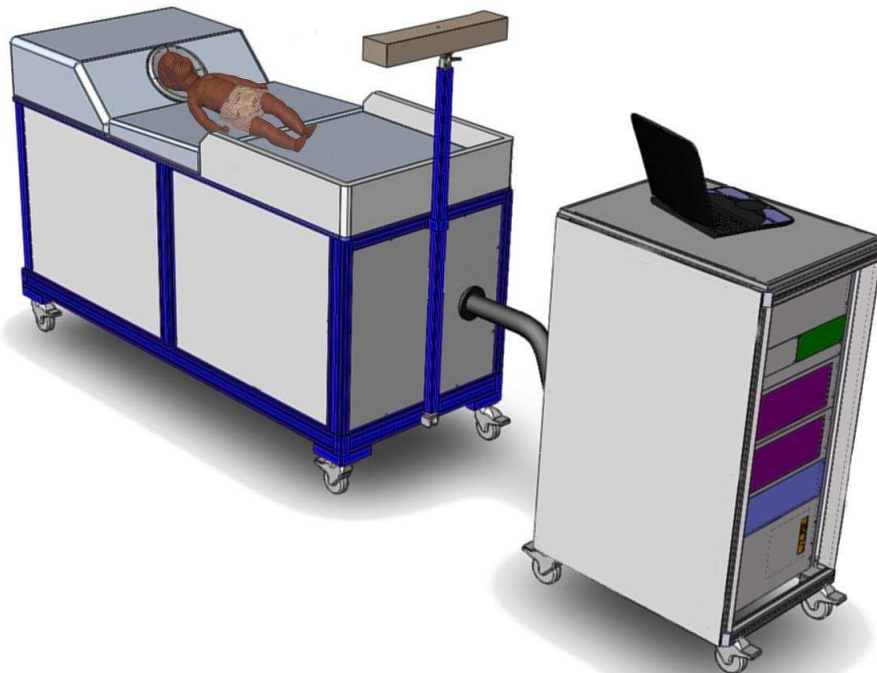


*Figure 2.3: The babySQUID cart.*

### 2.2.1 Sensor layout

The babySQUID sensor array consists of 76 axial gradiometers in a dense arrangement (Fig. 2.4). The closest distance between neighboring gradiometers is about 1.2 cm. The curvature of the array is designed to accommodate one hemisphere of an infant head. The slightly larger heads of older children (up to a few years of age) can also be studied.

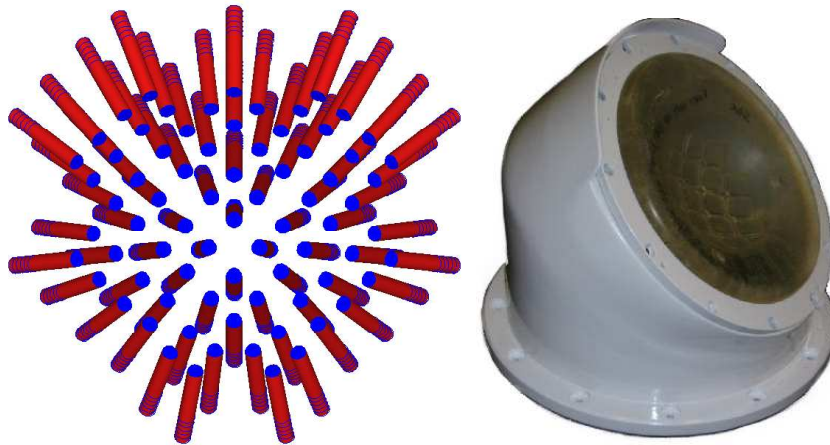


*Figure 2.4: The gradiometer array and the headrest.*

### 2.2.2 The gradiometers

Because of inductance considerations, the babySQUID gradiometers are somewhat more complicated than the schematic first-order gradiometer shown in Fig. 2.2. The coils have multiple turns, but the principle of operation is the same: the proximal coil picks up the signal and the distal coil compensates for homogenous disturbance fields. The signal coil has 12 turns in two layers, and the compensation coil has 6 turns in one layer.

Instead of suspending the gradiometers in a liquid helium bath, the babySQUID uses thermal conductors between the dewar and the gradiometers to cool them down. This has the advantage that the gradiometers can be brought very close to the subject: the distance between the signal coils and the headrest is only about 6 mm. This leads to an increased signal-to-noise ratio (the field of a current dipole falls off as  $1/r^2$ , so decreasing the distance has a large effect on field strength). Also, the design permits the sensor array to be oriented upwards.

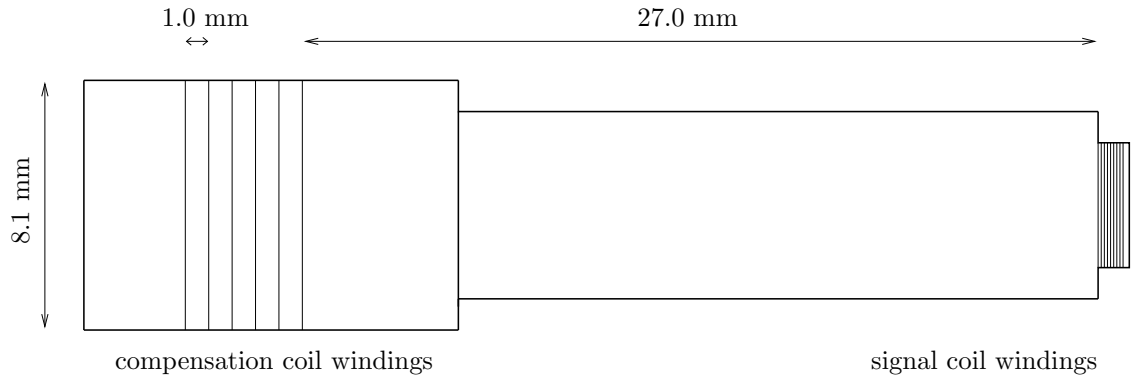


Figure 2.5: The babySQUID gradiometer (drawing not to scale). The baseline (closest distance between compensation coil and input coil windings) is 27.0 mm.

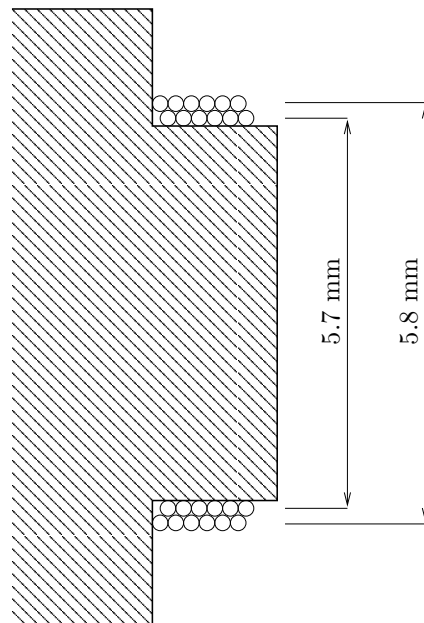


Figure 2.6: Cross section of the signal coil windings. The coil has 12 windings in two layers.

### 2.2.3 Noise cancellation

The aim of the babySQUID design is to be able to operate without magnetic shielding in noisy environments such as hospitals. In such an environment, lots of electric equipment is used and thus there are many potential sources of magnetic disturbances.

In the babySQUID, various noise cancellation methods are utilized to remove the disturbances from the measured data. There are 8 reference channels that measure the fields caused by external disturbance sources. The information provided by them can be used to cancel noise that is correlated between the reference channels and the gradiometers. Temporal filtering is used to remove noise that is outside the frequency range of interest. It is hoped that the SSS method studied in this work will provide additional noise cancellation.

# Chapter 3

## Methods

### 3.1 The forward problem

The forward problem is the calculation of the magnetic field caused by a known current source. We use the quasistatic approximation to make the calculations simpler. It is valid in neuromagnetism, as we are usually dealing with frequencies below 100 Hz [6]. In this approximation, the time-derivative terms are dropped from the Maxwell equations and the equations become

$$\nabla \cdot \mathbf{E} = \rho/\epsilon_0, \quad (3.1)$$

$$\nabla \times \mathbf{E} = 0, \quad (3.2)$$

$$\nabla \cdot \mathbf{B} = 0, \quad (3.3)$$

$$\nabla \times \mathbf{B} = \mu_0 \mathbf{J}. \quad (3.4)$$

where  $\mathbf{E}$ ,  $\mathbf{B}$  and  $\mathbf{J}$  are the electric field, the magnetic field and the electric current density, respectively, and  $\rho$  the electric charge density.

When considering current sources in the brain, it is useful to follow [6] and separate the current density into two parts:

$$\mathbf{J} = \mathbf{J}^p + \mathbf{J}^v. \quad (3.5)$$

Here  $\mathbf{J}^v$  is the volume current:  $\mathbf{J}^v = \sigma \mathbf{E}$ . The brain is thought as a homogenous conductor, and  $\sigma$  represents the macroscopic conductivity. The cellular level details are ignored. The primary current  $\mathbf{J}^p$  is then defined to

be everything else than macroscopic volume currents. Following this definition, it may be said that the neural activity gives rise to a primary current (due to electrochemical gradients) in the cells or in their vicinity, while the passive volume current flows everywhere in the conductor.

A widely used model for  $\mathbf{J}^P$  in neuromagnetism is the current dipole, which is a current spatially restricted to a single point. This model is clearly unphysical, but it is very useful as an equivalent source for localized unidirectional currents. The current density of the dipole is defined as

$$\mathbf{J}(\mathbf{r}) = \mathbf{Q}\delta(\mathbf{r} - \mathbf{r}_Q). \quad (3.6)$$

Here  $\mathbf{Q}$  is the dipole moment [Am],  $\mathbf{r}_Q$  the location of the dipole and  $\mathbf{r}$  the point where the field is computed.  $\delta(\mathbf{r})$  is the Dirac delta function.

We use current dipoles in free space as a model for disturbance sources. In this case, there are no volume currents and the expression for the field of the current dipole can be computed directly from Ampere's law:

$$\mathbf{B}(\mathbf{r}) = \frac{\mu_0}{4\pi} \frac{\mathbf{Q} \times (\mathbf{r} - \mathbf{r}_Q)}{(\mathbf{r} - \mathbf{r}_Q)^3}. \quad (3.7)$$

Of course, the space is not actually free, but it is realistic to assume that the fields are not distorted significantly in the vicinity of the MEG sensors, since in a real measurement situation there should not be any large objects with good conductivity there.

For simulating a source in the brain, it is more realistic to use a model with the current dipole inside a spherically symmetric volume conductor that represents the head. In this case, the magnetic field outside the sphere may be computed as

$$\mathbf{B}(\mathbf{r}) = \frac{\mu_0}{4\pi} \frac{F\mathbf{Q} \times \mathbf{r}_Q - (\mathbf{Q} \times \mathbf{r}_Q \cdot \mathbf{r})\nabla F}{F^2}, \quad (3.8)$$

where

$$F = a(ra + r^2 - \mathbf{r} \cdot \mathbf{r}_Q),$$

and  $\mathbf{a} = \mathbf{r} - \mathbf{r}_Q$ ,  $a = \|\mathbf{a}\|$ ,  $r = \|\mathbf{r}\|$ . This result is derived in [11]. Notice that the field outside the sphere does not depend on the radius or the radial

conductivity profile of the sphere, and the volume current does not feature explicitly in the calculation.

## 3.2 The SSS method

In this section, we develop the Signal Space Separation method starting from the solution to Laplace's equation. It is found that the series solution can be split into two parts in a way that is very relevant for an MEG measurement. The resulting terms are then discretized by into finite dimensional signal space vectors by considering a measurement given by a finite number of sensors, and finally a convenient matrix formalism is developed. We mostly follow the development presented in [14].

According to the fourth Maxwell's equation (3.4),  $\nabla \times \mathbf{B} = \mathbf{0}$  in a source free region. Therefore  $\mathbf{B}$  can be expressed as a gradient of a scalar potential  $V$ :

$$\mathbf{B} = -\nabla V. \quad (3.9)$$

Taking the divergence and noting that  $\nabla \cdot \mathbf{B} = 0$ ,  $V$  is found to satisfy Laplace's equation:

$$\nabla^2 V = 0. \quad (3.10)$$

We study the solution of this equation in spherical coordinates  $\mathbf{r} = (r, \theta, \phi)$ , where  $r$  is the radius from the origin,  $\theta$  is the polar angle measured from the positive z-axis, and  $\phi$  is the azimuthal angle measured from the positive x-axis. The general solution for a real  $V$  is

$$V(\mathbf{r}) = \sum_{l=0}^{\infty} \sum_{m=-l}^l \alpha_{lm} \frac{y_{lm}(\theta, \phi)}{r^{l+1}} + \sum_{l=0}^{\infty} \sum_{m=-l}^l \beta_{lm} r^l y_{lm}(\theta, \phi) \quad (3.11)$$

where  $\alpha_{lm}$  and  $\beta_{lm}$  are (real) coefficients and  $y_{lm}(\theta, \phi)$  is a real spherical surface harmonic. See Appendix A for definitions and derivation of the solution.

The key to the SSS algorithm is the  $r$  dependency of terms in Eq. 3.11. The  $1/r^{l+1}$  terms diverge at the origin, and they characterize sources that are closer to the center of the expansion than any of the measurement points. The  $r^l$  terms diverge at  $r = \infty$ , characterizing sources that are more distant

from the center of the expansion than any of the measurement points. The two source types are illustrated in Fig. 3.1, where sources in volume 1 are closer to the center of expansion than any of the sensors and sources in volume 3 are farther from it than any of the sensors.

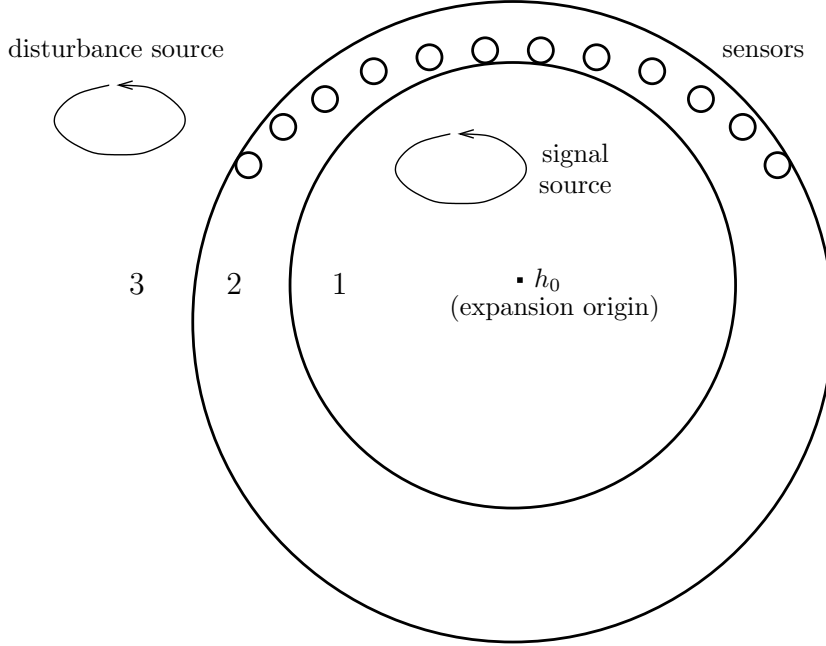


Figure 3.1: Geometry of the SSS reconstruction.

We call spheres that define volumes 1 and 3 the inner and outer convergence sphere, respectively. The radius of the inner convergence sphere is the minimum distance between the center of expansion and the sensor array, and the radius of the outer convergence sphere is the respective maximum distance.

Combining Eqs. 3.9 and 3.11, we find that in the quasistatic approximation, any magnetic field can be represented as

$$\mathbf{B}(\mathbf{r}) = -\sum_{l=0}^{\infty} \sum_{m=-l}^l \alpha_{lm} \nabla \left[ \frac{y_{lm}(\theta, \phi)}{r^{l+1}} \right] - \sum_{l=0}^{\infty} \sum_{m=-l}^l \beta_{lm} \nabla \left[ r^l y_{lm}(\theta, \phi) \right] \quad (3.12)$$

Now let us define the 76-dimensional signal space vector  $\mathbf{a}_{lm}$  as the response of the sensor array to  $-\nabla \left[ \frac{y_{lm}(\theta, \phi)}{r^{l+1}} \right]$ , and  $\mathbf{b}_{lm}$  as the response to  $-\nabla \left[ r^l y_{lm}(\theta, \phi) \right]$ . The complete sets of  $\mathbf{a}_{lm}$  and  $\mathbf{b}_{lm}$  span the subspaces corresponding to the sources inside volumes 1 and 3, respectively. Fields

caused by sources in volume 2 do not belong to either subspace, and therefore volume 2 should ideally be source-free. Of course, this condition cannot be satisfied in a practical measurement situation, as there will be currents flowing everywhere in the body of a human subject. For the method to work, it is sufficient that the field caused by sources in volume 2 is small enough compared to the fields caused by sources in volumes 1 and 3.

According to Eq. 3.12, any signal space vector can be represented as

$$\boldsymbol{\phi} = \sum_{l=0}^{\infty} \sum_{m=-l}^l \alpha_{lm} \mathbf{a}_{lm} + \sum_{l=0}^{\infty} \sum_{m=-l}^l \beta_{lm} \mathbf{b}_{lm}. \quad (3.13)$$

However, in practice a finite number of terms is sufficient to represent any measured magnetic field. The sources are always separated from the sensors by a certain minimum distance, so there is a limit to the spatial frequencies needed to represent the signal vectors produced by them (terms with higher  $l$  in Eq. 3.13 correspond to higher spatial frequencies). If the cutoff for  $l$  is chosen to be  $L_a$  for the  $\mathbf{a}_{lm}$  vectors and  $L_b$  for the  $\mathbf{b}_{lm}$  vectors, we obtain

$$\boldsymbol{\phi} = \sum_{l=1}^{L_a} \sum_{m=-l}^l \alpha_{lm} \mathbf{a}_{lm} + \sum_{l=1}^{L_b} \sum_{m=-l}^l \beta_{lm} \mathbf{b}_{lm}. \quad (3.14)$$

Here the  $l = 0$  terms have been left out, because they represent fields of magnetic monopole sources. Since there are  $2l + 1$  basis vectors in each basis for every  $l$ , the number of basis vectors  $N'$  is

$$N' = \sum_{l=1}^{L_a} (2l + 1) + \sum_{l=1}^{L_b} (2l + 1) = L_a^2 + 2L_a + L_b^2 + 2L_b. \quad (3.15)$$

However, the three  $\mathbf{b}_{lm}$  vectors for  $l = 1$  are zero for instruments containing only gradiometers, since these vectors represent spatially homogenous fields. Consequently, the dimension  $N$  of the SSS basis for gradiometer arrays is

$$N = N_a + N_b = L_a^2 + 2L_a + L_b^2 + 2L_b - 3. \quad (3.16)$$

Eq. 3.14 can be expressed in matrix form as

$$\boldsymbol{\phi} = \mathbf{S}\mathbf{x}, \quad (3.17)$$

where

$$\mathbf{S} = [\mathbf{A} \ \mathbf{B}] = [\mathbf{a}_{1,-1}, \mathbf{a}_{1,0}, \mathbf{a}_{1,1}, \dots, \mathbf{a}_{L_a, L_a} \ \mathbf{b}_{1,-1}, \mathbf{b}_{1,0}, \mathbf{b}_{1,1}, \dots, \mathbf{b}_{L_b, L_b}] \quad (3.18)$$

is the SSS matrix with the basis vectors as its columns, and

$$\mathbf{x} = [\mathbf{x}_a \ \mathbf{x}_b]^\top = [\alpha_{1,-1}, \alpha_{1,0}, \alpha_{1,1}, \dots, \alpha_{L_a, L_a} \ \beta_{2,-2}, \beta_{2,-1}, \beta_{2,0}, \dots, \beta_{L_b, L_b}]^\top \quad (3.19)$$

is a coefficient vector.

The least squares solution  $\hat{\mathbf{x}}$  for any measured  $\phi$  is

$$\hat{\mathbf{x}} = \mathbf{S}^\dagger \phi. \quad (3.20)$$

where  $\mathbf{S}^\dagger$  is the pseudoinverse of  $\mathbf{S}$  (discussed in the next section). The dimension of the signal space vectors equals the number of sensors in the array. Thus, if  $N < 76$ , the problem will be overdetermined and the solution is unique.

The choice of the center of expansion  $\mathbf{h}_0$  is important. By placing  $\mathbf{h}_0$  close to the sensor array, the inner convergence sphere becomes smaller, which places restrictions on the allowed source locations. However, the reconstruction of sources will be possible with smaller  $L_a$ . This makes the problem more stable numerically and easier to solve.

After solving for  $\hat{\mathbf{x}}$ , the signal space vectors corresponding to internal and external sources may be reconstructed as

$$\begin{aligned} \hat{\phi}_{int} &= \mathbf{A} \hat{\mathbf{x}}_a \\ \hat{\phi}_{ext} &= \mathbf{B} \hat{\mathbf{x}}_b. \end{aligned} \quad (3.21)$$

The terms ‘‘internal source’’ and ‘‘external source’’ refer to sources in volume 1 and volume 3, respectively (Fig. 3.1). It turns out that the simple pseudoinverse solution of Eq. 3.20 usually does not give reasonable answers when the method is applied to the babySQUID. This means that the problem is ill-conditioned, and regularization methods are needed.

### 3.3 Regularization

In this section, we introduce the pseudoinverse and discuss the problem of ill-conditioned matrices. We then briefly introduce some regularization methods that can be used to deal with this problem. The truncated singular value decomposition (TSVD) and modified truncated singular value decomposition (MTSVD) methods are not really utilized in this work, but a short discussion of them is useful as it leads naturally to the development of the piecewise polynomial TSVD (PP-TSVD) method, which was found to be very useful. More details can be found in the manual of Hansen's regularization package [8] and his PP-TSVD paper [9].

#### 3.3.1 The pseudoinverse and SVD

Consider the overdetermined system of linear equations

$$\mathbf{Ax} = \mathbf{b}, \quad (3.22)$$

where  $\mathbf{A} \in \mathbb{R}^{m \times n}$ ,  $\mathbf{x} \in \mathbb{R}^n$ ,  $\mathbf{b} \in \mathbb{R}^m$  and  $m > n$ .

We can find a least squares solution by minimizing

$$\|\mathbf{Ax} - \mathbf{b}\|^2 = (\mathbf{Ax} - \mathbf{b})^\top (\mathbf{Ax} - \mathbf{b}) = (\mathbf{x}^\top \mathbf{A}^\top \mathbf{Ax} - 2\mathbf{x}^\top \mathbf{A}^\top \mathbf{b} + \mathbf{b}^\top \mathbf{b}). \quad (3.23)$$

Taking the derivative with respect to  $\mathbf{x}$  and setting it to zero yields

$$\begin{aligned} \mathbf{A}^\top \mathbf{Ax} &= \mathbf{A}^\top \mathbf{b} \\ \mathbf{x} &= (\mathbf{A}^\top \mathbf{A})^{-1} \mathbf{A}^\top \mathbf{b}. \end{aligned} \quad (3.24)$$

This is commonly denoted  $\mathbf{x} = \mathbf{A}^\dagger \mathbf{b}$ , where  $\mathbf{A}^\dagger = (\mathbf{A}^\top \mathbf{A})^{-1} \mathbf{A}^\top$  is the pseudoinverse of  $\mathbf{A}$ .

For ill-conditioned problems, which arise quite often in practice, a numerically computed pseudoinverse solution may become useless because of its sensitivity to measurement and roundoff errors. To study this issue, we express  $\mathbf{A}$  as its singular value decomposition:

$$\mathbf{A} = \mathbf{U}\mathbf{\Sigma}\mathbf{V}^\top, \quad (3.25)$$

where  $\mathbf{U} = (\mathbf{u}_1, \mathbf{u}_2, \dots, \mathbf{u}_m)$  and  $\mathbf{V} = (\mathbf{v}_1, \mathbf{v}_2, \dots, \mathbf{v}_n)$  are orthogonal square matrices, and  $\Sigma \in \mathbb{R}^{m \times n}$  is a diagonal matrix the singular values  $\sigma_1, \dots, \sigma_n$  in nonincreasing order on its diagonal. The previous equation may be written as

$$\mathbf{A} = \sum_{i=1}^n \mathbf{u}_i \sigma_i \mathbf{v}_i^T. \quad (3.26)$$

Inserting the decomposition (3.25) into the definition of pseudoinverse (Eq. 3.24) gives

$$\begin{aligned} \mathbf{x} &= (\mathbf{V}\Sigma^T\mathbf{U}^T\mathbf{U}\Sigma\mathbf{V}^T)^{-1}\mathbf{V}\Sigma^T\mathbf{U}^T\mathbf{b} \\ &= \mathbf{V}(\Sigma^T\Sigma)^{-1}\mathbf{V}^T\mathbf{V}\Sigma^T\mathbf{U}^T\mathbf{b} \\ &= \mathbf{V}(\Sigma^T\Sigma)^{-1}\Sigma^T\mathbf{U}^T\mathbf{b}. \end{aligned} \quad (3.27)$$

The steps follow from the orthogonality of  $\mathbf{U}$  and  $\mathbf{V}$  ( $\mathbf{U}^{-1} = \mathbf{U}^T$ ,  $\mathbf{V}^{-1} = \mathbf{V}^T$ ).

Because  $\Sigma$  has nonzero values only on its diagonal, it is easy to see that this expression equals

$$\mathbf{x} = \sum_{i=1}^n \frac{\mathbf{u}_i^T \mathbf{b}}{\sigma_i} \mathbf{v}_i. \quad (3.28)$$

Here it is assumed that  $\mathbf{A}$  has no singular values equal to zero. If this is not the case,  $\mathbf{A}$  is rank deficient. Then the least squares solution is not unique, as  $\mathbf{A}$  has a nontrivial nullspace  $\text{Null}\{\mathbf{A}\} = \{\mathbf{v} : \mathbf{A}\mathbf{v} = \mathbf{0}\}$ , and adding any  $\mathbf{v} \in \text{Null}\{\mathbf{A}\}$  to  $\mathbf{x}$  will not change  $\|\mathbf{A}\mathbf{x} - \mathbf{b}\|$ .

An ill-conditioned problem is characterized by singular values smoothly decaying towards zero. This causes problems in numerical calculations as Eq. 3.28 becomes dominated by terms corresponding to the smallest singular values, and errors in these terms are “blown up” in the solution. To characterize the condition of the matrix, we define the condition number as the ratio of the largest and the smallest singular values:

$$C_{cond} = \sigma_1/\sigma_n. \quad (3.29)$$

The idea of regularization methods is effectively to introduce a filter factor  $f_i$  in Eq. 3.28, so that the new solution is

$$\mathbf{x} = \sum_{i=1}^n f_i \frac{\mathbf{u}_i^\top \mathbf{b}}{\sigma_i} \mathbf{v}_i. \quad (3.30)$$

The purpose of  $f_i$  is to reduce the error-prone contribution of terms corresponding to small  $\sigma_i$ .

### 3.3.2 Tikhonov regularization

Tikhonov regularization is based on seeking an  $\mathbf{x}$  that minimizes a linear combination of the residual norm  $\|\mathbf{A}\mathbf{x} - \mathbf{b}\|$  and a constraint:

$$\min\{\|\mathbf{A}\mathbf{x} - \mathbf{b}\|^2 + \lambda^2\|\mathbf{L}\mathbf{x}\|^2\}. \quad (3.31)$$

If  $\mathbf{L} = \mathbf{I}$ , the constraint just minimizes the norm of  $\mathbf{x}$ . Another choice is a discrete approximation to a derivative operator, which leads to a smoother solution. The choice of the parameter  $\lambda$  controls the amount of regularization. A small  $\lambda$  emphasizes minimization of the residual norm, corresponding to a small amount of regularization. Conversely, a large  $\lambda$  emphasizes the constraint.

### 3.3.3 TSVD

The TSVD (truncated singular value decomposition) solution is obtained by approximating  $\mathbf{A}$  with a rank deficient matrix  $\mathbf{A}_k$ , using only the first  $k$  terms from Eq. (3.26):

$$\mathbf{A}_k = \sum_{i=1}^k \mathbf{u}_i \sigma_i \mathbf{v}_i^\top. \quad (3.32)$$

Since  $\mathbf{A}_k$  is now rank deficient, the solution to the new problem

$$\min\|\mathbf{A}_k \mathbf{x} - \mathbf{b}\| \quad (3.33)$$

is no longer unique, as discussed before. However, a minimum norm solution is given by

$$\mathbf{x}_k = \sum_{i=1}^k \frac{\mathbf{u}_i^\top \mathbf{b}}{\sigma_i} \mathbf{v}_i. \quad (3.34)$$

This is the minimum norm solution, because  $\text{Null}\{\mathbf{A}_k\}$  is spanned by the vectors  $(\mathbf{v}_{k+1}, \dots, \mathbf{v}_n)$ , which are orthogonal to  $\mathbf{x}_k$ , so adding any  $\mathbf{v} \in \text{Null}\{\mathbf{A}_k\}$ ,  $\mathbf{v} \neq 0$  to  $\mathbf{x}_k$  will increase its norm.

Therefore,  $\mathbf{x} = \mathbf{x}_k$  is the solution to

$$\min \|\mathbf{x}\| \quad \text{subject to} \quad \min \|\mathbf{A}_k \mathbf{x} - \mathbf{b}\|. \quad (3.35)$$

This corresponds to setting  $f_i = 0$  for  $i > k$  and  $f_i = 1$  otherwise in Eq. 3.30. The parameter  $k$  controls the amount of regularization: smaller  $k$  will correspond to smaller  $\|\mathbf{x}\|$  (again because of orthogonality of vectors  $\mathbf{v}_i$ ), but the approximation  $\mathbf{A}_k \approx \mathbf{A}$  worsens with decreasing  $k$ .

### 3.3.4 MTSVD

In many applications, minimization of  $\|\mathbf{L}\mathbf{x}\|^2$ , rather than  $\|\mathbf{x}\|^2$ , is desired.  $\mathbf{L}$  is usually an approximate derivative operator, as discussed in the context of the Tikhonov problem. MTSVD (modified TSVD) replaces the TSVD minimization problem (Eq. 3.33) by

$$\min \|\mathbf{L}\mathbf{x}\|^2 \quad \text{subject to} \quad \min \|\mathbf{A}_k \mathbf{x} - \mathbf{b}\|. \quad (3.36)$$

From the TSVD problem, we know that  $\mathbf{x} = \mathbf{x}_k$  (given by Eq. 3.34) is the solution to  $\min \|\mathbf{A}_k \mathbf{x} - \mathbf{b}\|$ . We modify  $\mathbf{x}_k$  by adding a vector from  $\text{Null}\{\mathbf{A}_k\}$ , so that the already minimized norm  $\|\mathbf{A}_k \mathbf{x}_k - \mathbf{b}\|$  will not change. Define  $\mathbf{K}$  as a column matrix formed by the vectors spanning  $\text{Null}\{\mathbf{A}_k\}$ :

$$\mathbf{K} = (\mathbf{v}_{k+1}, \dots, \mathbf{v}_n). \quad (3.37)$$

Now, the modified solution is  $\mathbf{x}_k - \mathbf{K}\boldsymbol{\omega}$ , where  $\boldsymbol{\omega}$  is a coefficient vector. Inserting the modified solution in Eq. 3.36, we seek  $\boldsymbol{\omega}$  that solves the problem

$$\min \|\mathbf{L}\mathbf{x}_k - \mathbf{L}\mathbf{K}\boldsymbol{\omega}\|^2. \quad (3.38)$$

Using Eq. 3.24, we obtain the least-squares solution:

$$\boldsymbol{\omega} = (\mathbf{LK})^\dagger \mathbf{L}\mathbf{x}_k. \quad (3.39)$$

The solution to Eq. 3.36 is therefore given by

$$\mathbf{x}_{MTSVD} = \mathbf{x}_k - \mathbf{K}(\mathbf{LK})^\dagger \mathbf{L}\mathbf{x}_k. \quad (3.40)$$

### 3.3.5 PP-TSVD

PP-TSVD (piecewise polynomial TSVD) is a new method introduced by Hansen and Mosegaard [9]. The motivation behind it is that the minimization of the 2-norm in TSVD and MTSVD tends to produce smooth solutions. Smooth solutions are often desirable, but in some problems the solutions tend to have sharp edges. For such problems, it is more appropriate to minimize the 1-norm (denoted  $\|\cdot\|_1$ ) of the solution. The minimization problem in PP-TSVD is

$$\min \|\mathbf{L}\mathbf{x}\|_1 \quad \text{subject to} \quad \min \|\mathbf{A}_k \mathbf{x} - \mathbf{b}\|. \quad (3.41)$$

We can modify the solution as in the MTSVD method:  $\mathbf{x}_{PPTSVD} = \mathbf{x}_k - \mathbf{K}\boldsymbol{\omega}$ . However, because of the 1-norm, the resulting minimization problem

$$\min \|\mathbf{L}\mathbf{x}_k - \mathbf{LK}\boldsymbol{\omega}\|_1 \quad (3.42)$$

does not have a closed form solution, but has to be solved numerically.

## 3.4 Implementation of the simulation

The SSS simulation was constructed in Matlab environment. It allows the user to specify an arbitrary number of sources with desired locations and orientations. The sources are current dipoles in free space or inside a spherical head model. The simulation computes the resulting magnetic field as measured by the babySQUID gradiometer array and then solves the SSS reconstruction problem using a specified regularization method.

### 3.4.1 Integration of the magnetic fields

To integrate the simulated magnetic field over the pickup coils, a numerical integration procedure is needed. The numerical integration approximation is of the form

$$\int_C \mathbf{B} \cdot d\mathbf{A} \approx \sum_{i=1}^{N_p} w_i \mathbf{B}(\mathbf{p}_i), \quad (3.43)$$

where  $C$  represents the area determined by the pickup coil,  $\mathbf{p}_i$  are the  $N_p$  points used in the approximation (usually inside  $C$ ) and  $w_i$  are the corresponding weights. The surface elements  $d\mathbf{A}$  are directed so that a field emerging from the head towards the sensor array results in a positive measured value.

Optimal  $\mathbf{p}_i$  and  $w_i$  may be derived by different methods and are tabulated in references such as [12]. In general, different kinds of approximations are optimal for different integrands. For the purposes of this simulation, formulas with 12, 19, 41 and 99 points were tested. They were taken from [12] and [5]. The 19-point formula was found to be sufficiently accurate even for the most complex basis vectors.

The babySQUID has two coils with multiple turns on each gradiometer. The output of a gradiometer  $b_i$  is computed as

$$b_i = \frac{1}{12} \sum_{j=1}^{12} B_{si}^j - \frac{1}{6} \sum_{j=1}^6 B_{ci}^j \quad (3.44)$$

where  $B_{si}^j$  and  $B_{ci}^j$  are the field values given by the signal coil and the  $j$ th compensation coil of the  $i$ th gradiometer, respectively. They are computed using the integration formula 3.43 and dividing by the area of the coil.

For simplicity, the field values measured by the gradiometers are given as fT in this work. Another possibility would be to divide the  $b_i$  by the gradiometer baseline and report the spatial gradient (fT/cm).

### 3.4.2 Regularization

The regularization methods presented in the previous section are available in the simulation. Code from the Regularization Tools software package by

Per Hansen [8] and the PP-TSVD implementation available on his website [7] were used.

It should be noted that smoothness is not a desired property for the solutions for the coefficient vector  $\hat{\mathbf{x}}$  (the solution often consists of just a few spikes). Therefore, the operator  $\mathbf{L}$  is chosen to be identity in all regularization formulas. This means that the norm of the solution is minimized instead of the norm of its derivative, which allows for nonsmooth solutions. The MTSVD method is not tested for the same reason (it is just a generalization of TSVD for non-identity  $\mathbf{L}$ ).

### 3.4.3 Simulated sensor noise

To simulate sensor noise, white Gaussian noise with a variance of  $\sigma_N^2$  is added to the signal vectors before applying SSS. A standard deviation of 10 fT was chosen for the noise.

# Chapter 4

## Results

This chapter presents the results of the simulations. After defining coordinate systems and some parameters in Section 4.1, the optimal regularization method is found in Section 4.2. The regularized Signal Space Separation method is tested in Section 4.3. Section 4.4 considers the effect of different nonideal properties of the real instrument.

### 4.1 Preliminary issues

First, the coordinate system for the sensor array is established. The chosen Cartesian system is illustrated in Fig. 4.1. For clarity, the compensation coils are not drawn in this or subsequent figures. All coordinates given in this chapter will refer to this system.

We will focus on the overdetermined problem, choosing  $N < 76$  for the number of basis vectors. From Eq. 3.16, we see that the choice  $L_a = 6$ ,  $L_b = 4$  yields  $N = 69$  ( $N_a = 48$  and  $N_b = 21$ ). Another potentially useful choice is  $L_a = 7$ ,  $L_b = 3$  ( $N_a = 63$ ,  $N_b = 12$ ).  $L_a$  is required to be larger than  $L_b$ , since the internal sources tend to be close to the sensor array and give rise to fields with higher spatial frequencies than the external sources.

In a simulation, the true theoretical field of the signal source is known, so it is possible to study the quality of the reconstruction. For this, we use the normalized root mean square (NRMS) error, defined as

$$\varepsilon = \sqrt{\frac{\sum_i (\phi_i - \hat{\phi}_i)^2}{\sum_i \phi_i^2}}. \quad (4.1)$$

---

Here  $\phi_i$  and  $\hat{\phi}_i$  are the  $i$ th components of the true and SSS reconstructed signal vectors, respectively. In computing the NRMS error, we include only channels (signal vector components) where the signal strengths are more than 20 % of the maximum in that signal vector. Computed this way, the NRMS gives a more realistic picture of reconstruction of the important signal features.

In the test cases, the sources are listed in tables that include the coordinates and the dipole moment of each source, as well as location, which can be internal, external or intermediate. “Intermediate” refers to sources that are in the space between the two convergence spheres (volume 2 in Fig. 3.1).

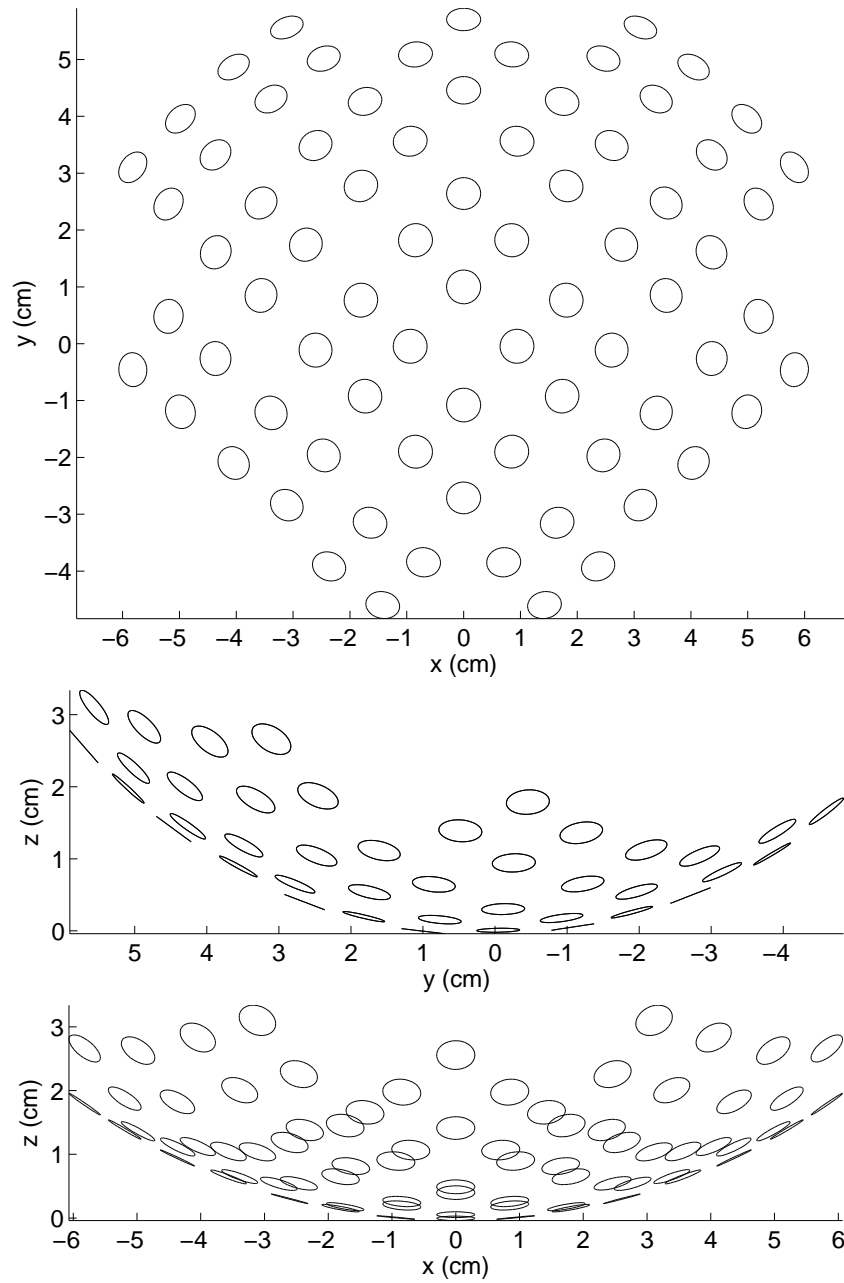


Figure 4.1: The babySQUID sensor array, as seen from above, from the side, and from the front.

## 4.2 Regularization

We illustrate the performance of the different regularization methods by the simple example of reconstructing a signal source 1 cm away from the sensor array, while one disturbance source about 1.7 m from the sensors is present. The signal source is located inside a sphere model centered at (0.00, 0.00, 0.05) (we denote the center of the sphere model by  $\mathbf{s}_0$  from now on). The magnitudes of the dipoles are chosen so that the maximum magnitude of the disturbance over the sensor array is about twice the maximum magnitude of the signal.

location	$x(\text{m})$	$y$	$z$	$Q_x(\text{Am})$	$Q_y$	$Q_z$
internal	0.00	0.01	0.008	$1.00 \cdot 10^{-9}$	$0.40 \cdot 10^{-9}$	0.00
external	1.00	1.00	1.00	$1.00 \cdot 10^{-3}$	$2.00 \cdot 10^{-3}$	$1.00 \cdot 10^{-3}$

Table 4.1: Dipoles for the regularization example.

$\mathbf{h}_0$	(0.00, 0.00, 0.04)
$\mathbf{s}_0$	(0.00, 0.00, 0.05)
$L_a$	7
$L_b$	3

Table 4.2: SSS parameters for the regularization example.

In this case, the condition number of the basis vector matrix  $S$  (Eq. 3.17) is about  $4 \cdot 10^{16}$ , which clearly makes the pseudoinverse solution useless. The Tikhonov ( $\lambda = 0.02$ ) and TSVD ( $k=26$ ) solutions are better, but the reconstruction error  $\varepsilon$  cannot be reduced much below 1.00, so these solutions are not useful either. The PP-TSVD solution with an optimal value of  $k = 46$  gives  $\varepsilon = 0.10$ , which corresponds to a good reconstruction (Fig. 4.2). A representative result obtained with Tikhonov regularization ( $\varepsilon = 1.07$ ) is shown in Fig. 4.3.

More complicated source configurations only increase the difference between PP-TSVD and the other methods, so the conclusion is that PP-TSVD is the only usable reconstruction method of those considered. This is due to its ability to reconstruct solutions with sharp features more accurately than the other methods.

The optimal choice of the regularization parameter  $k$  for PP-TSVD depends on the choice of  $\mathbf{h}_0$ ,  $L_a$  and  $L_b$  but not significantly on the source configuration. Therefore, for given parameters, a good predetermined value of  $k$

may be used for all source configurations. This is crucial for the practical applicability of the method, since in real measurement, the reconstruction error cannot be determined and  $k$  cannot be optimized.

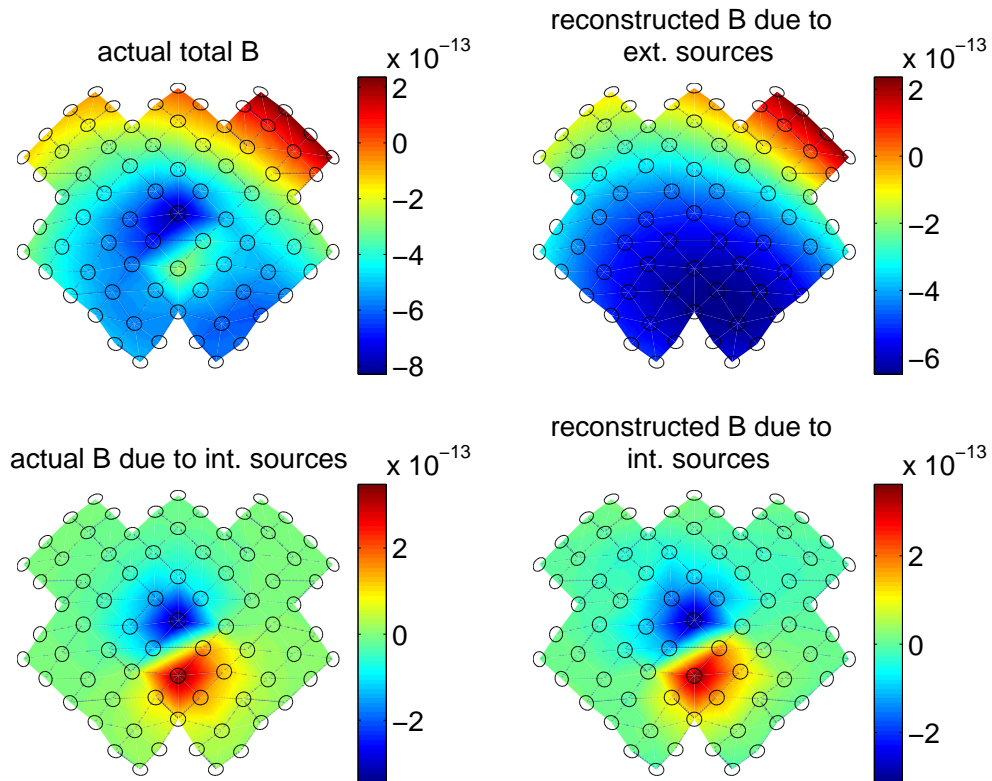


Figure 4.2: Example of a PP-TSVD regularized SSS reconstruction. In the unprocessed data, the dipole field of the internal source is obscured by the field of the external source (above left). The SSS method is able to separate the two sources and reconstruct the field of the internal source faithfully (lower left and right).

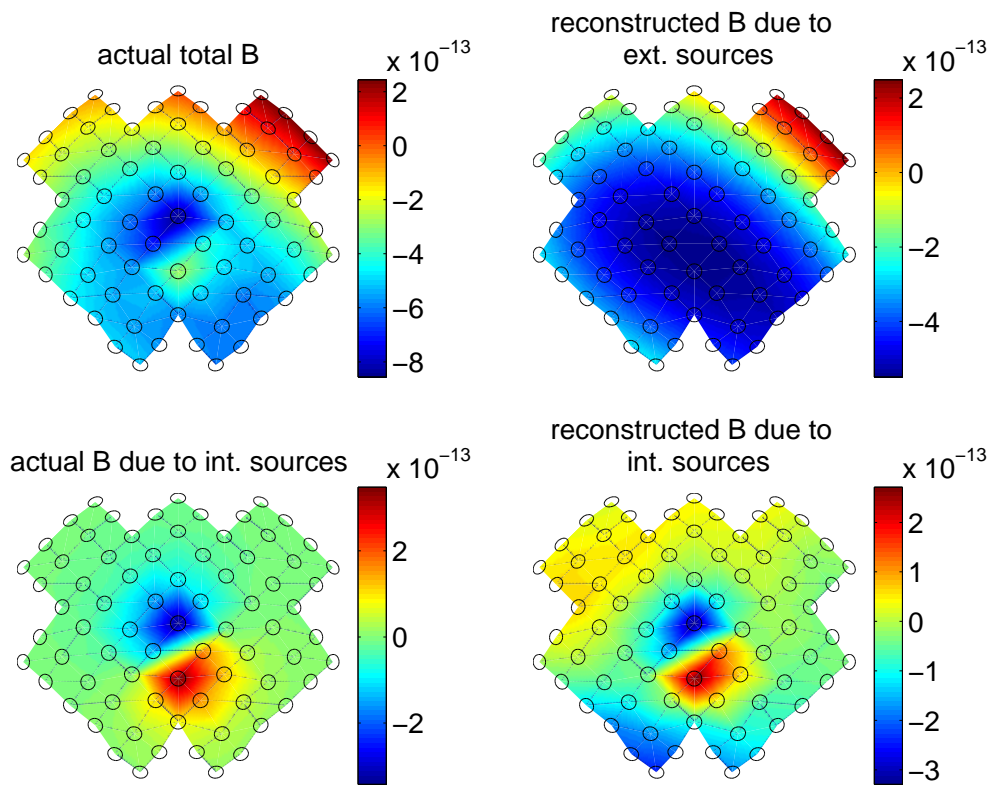


Figure 4.3: The best Tikhonov regularized reconstruction (see also Fig. 4.2). The dipole pattern is still visible in the correct position, but its amplitude is distorted.

### 4.2.1 Reconstruction speed

One problem with PP-TSVD regularization is that the solution requires a lot of computing power. With the current implementation of the algorithm, a typical reconstruction takes about 0.25 seconds on a 3 GHz PIII computer. Filtering one data segment of length  $T$  (seconds) with a sampling rate of  $f_s$  (Hz) then takes  $f_s T/4$  seconds. For  $f_s=1000$  Hz, the required time is  $250T$  seconds; one minute of data takes over four hours to process. For processing time-locked data segments (e.g. responses to visual stimuli), whose duration is usually less than one second, this is not a serious problem. However, processing long segments of raw data is very time-consuming, and real-time processing during the measurement is clearly not possible. It may be possible to increase the speed of the PP-TSVD implementation in [7], but the method will always be computationally quite demanding, as it requires solving an optimization problem.

### 4.2.2 Limitations imposed by the SSS geometry

In the regularization example, the radius of the inner convergence sphere was about 4 cm. This limits the locations of sources that can be reconstructed, since the curvature radius of the sensor array is about twice as large. We would like to use a larger convergence sphere if possible. But as the inner convergence sphere gets larger, basis vectors with increasingly high spatial frequency are required to represent the fields of sources close to the sensor array. For  $L_a=6$ , the upper limit for the radius of the sphere seems to be around 4 cm. Beyond that, even simple reconstructions start to fail. One approach to dealing with this is to increase the number of basis vectors beyond the number of channels and attempt to solve the resulting under-determined problem. Unfortunately, this does not work in practice: the problem becomes too difficult to solve even with regularization. Another possibility is to place  $\mathbf{h}_0$  closer to the source, if the source is reasonably limited in spatial extent and its approximate location is known.

## 4.3 Evaluations of the regularized SSS method

### 4.3.1 External sources at different distances

Next, we tested the ability of the regularized SSS to separate internal sources from external sources at different distances from the sensor array. For each distance, one random external source and internal source were generated.

The internal dipole was always located at the position (0.00, 0.00, 0.008). It had random orientation in the xy plane, and its field was normalized to have a maximum strength of 1 pT at the sensors. This ensures a constant signal-to-noise ratio. 1 pT is a source strength typically expected for infant measurements.

The external source was located at random angle from the sensor array ( $\theta$  and  $\phi$  uniformly distributed between  $\pi$  and  $2\pi$ , respectively) at a distance of  $d$  from origin. It was randomly oriented and normalized so that the maximum strength of its field, as measured by the sensor array, was  $D$  times the maximum strength of the internal field. For each distance, 20 pairs of sources were generated and separated by SSS. The NRMS values for the internal source were then averaged for each distance. Figures 4.4–4.7 show the average reconstruction error as a function of distance for different relative field strengths  $D$  and different SSS parameters.

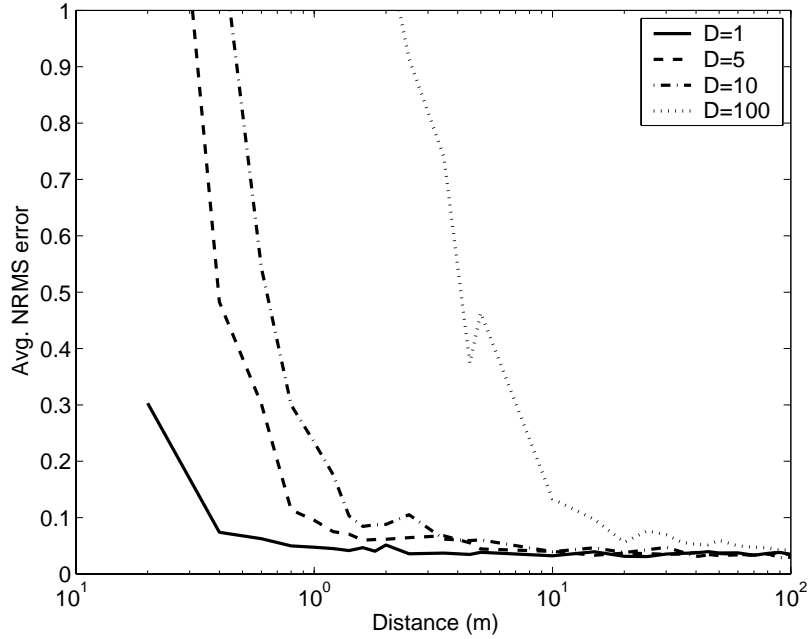


Figure 4.4: The average NRMS error for the reconstruction of the internal (signal) source, plotted as a function of the distance of the external (disturbance) source from the sensor array. The SSS parameters were  $L_a=6$ ,  $L_b=3$ ,  $r_{int}=3$  cm.

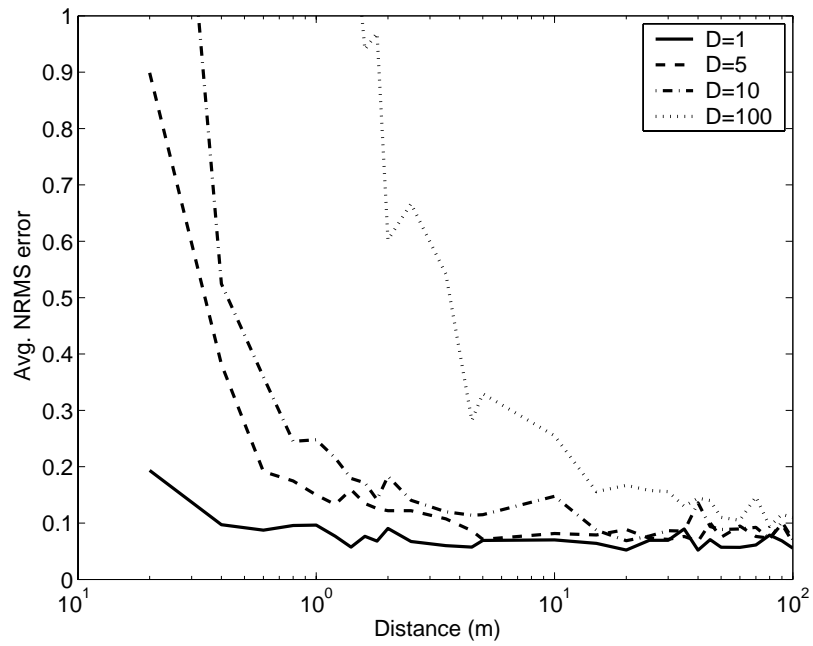


Figure 4.5: Reconstruction error for  $L_a=6$ ,  $L_b=4$ ,  $r_{int}=3$  cm (see Fig. 4.4)

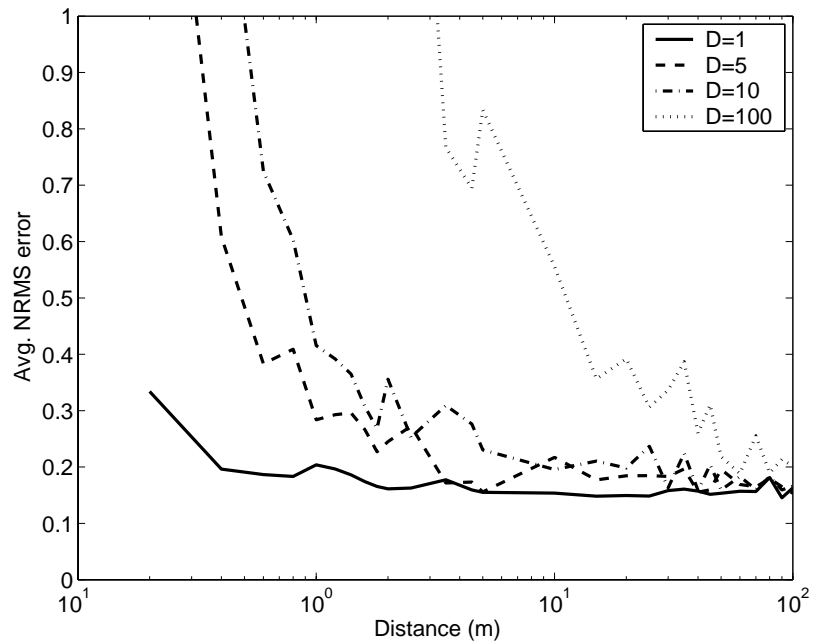


Figure 4.6: Reconstruction error for  $L_a=6$ ,  $L_b=4$ ,  $r_{int}=4$  cm (see Fig. 4.4)

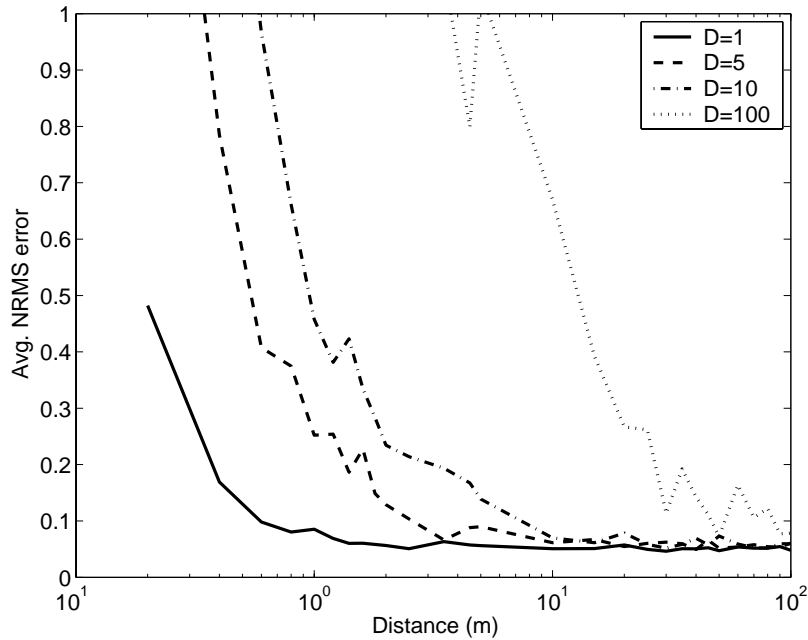


Figure 4.7: Reconstruction error for  $L_a=7$ ,  $L_b=3$ ,  $r_{int}=4$  cm (see Fig. 4.4)

Comparing the first two figures, we see that increasing  $L_b$  from 3 to 4 marginally improves the rejection of sources close to the sensor array. For sources farther away, the error is actually increased. The reason is that increasing the number of basis vectors makes the conditioning of the problem worse.

Fig. 4.6 shows that increasing  $r_{int}$  to 4 cm without increasing  $L_a$  worsens the reconstruction quality. This is seen also in the difference between figures 4.6 and 4.7.

The most useful configurations are  $L_a=6$ ,  $L_b=3$ ,  $r_{int}=3$  cm and  $L_a=7$ ,  $L_b=3$ ,  $r_{int}=4$  cm. The former gives better results (especially for close sources) but puts more restrictions on the possible source locations.

In general, it may be concluded that the “shielding factor” (maximum  $D$  that still allows rejection of the external source) is 1–5 for close sources (1 m from sensor array), between 10 and 100 for sources 10 m away, and at least 100 for sources that are 40 m or farther from the sensors. Rejection of sources closer than 1 m does not work very well, mostly because  $L_b$  cannot be increased beyond 4 (without reducing  $L_a$  and making the internal convergence sphere impractically small).

An approximation of the shielding factor can be computed by removing the internal source and seeing how much the field of the external source “leaks” into the reconstruction (of course, the reconstructed field of the internal source should ideally be zero). The shielding factor  $F$  is here defined as

$$F = -10 \log \frac{\max |\hat{\phi}_{int}|}{\max |\phi_{ext}|} \quad (4.2)$$

where  $\hat{\phi}_{int}$  is the internal field reconstruction and  $\phi_{ext}$  the measured external field. The average shielding factor for a randomly placed 1 nT external source at different distances is plotted in Fig. 4.8. The sources were placed in the same way as in the NRMS computations and results for 20 sources were averaged at each distance. The SSS configuration was  $L_a=7$ ,  $L_b=3$ ,  $r_{int}=4$  cm.

Computed this way, the shielding factor estimate gives a somewhat optimistic picture when compared with the NRMS results. For example, the shielding factor at 1 m is about 44, but Fig. 4.7 shows that a disturbance field with  $D=44$  at 1 m would result in an inaccurate reconstruction for the internal source. However, the shielding factor changes consistently with the NRMS, quickly getting worse when the external source is moved close to the

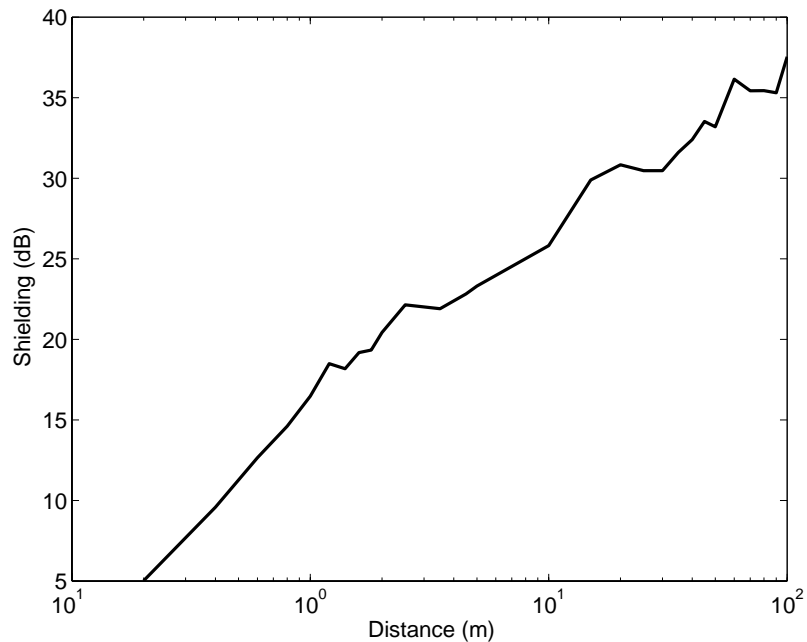


Figure 4.8: The estimated shielding factor.

sensor array.

### 4.3.2 Sources in the intermediate space

For practical application of the method, it is important to know what happens to the fields of sources that are located in the intermediate space. It turns out that they can still be reconstructed, at least roughly. To demonstrate this, a single source was placed at different positions while  $\mathbf{h}_0$  was kept close to the center of the array. The SSS parameters used are listed in Table 4.3 and the sources in Table 4.4.

$\mathbf{h}_0$	(0.00, 0.00, 0.04)
$\mathbf{s}_0$	(0.00, 0.00, 0.05)
$L_a$	7
$L_b$	3

Table 4.3: SSS parameters used in the reconstruction of the intermediate sources.

location	$x$ (m)	$y$	$z$	$Q_x$ (Am)	$Q_y$	$Q_z$	NRMS
interm.	0.03	0.00	0.013	$1.00 \cdot 10^{-9}$	$1.00 \cdot 10^{-9}$	0.00	0.32
interm.	0.04	0.00	0.017	$1.00 \cdot 10^{-9}$	$1.00 \cdot 10^{-9}$	0.00	0.77
interm.	0.03	-0.03	0.023	$1.00 \cdot 10^{-9}$	$1.00 \cdot 10^{-9}$	0.00	0.51
interm.	0.00	0.04	0.021	$1.00 \cdot 10^{-9}$	$1.00 \cdot 10^{-9}$	0.00	0.47
external	-1.03	4.77	-1.09	0.018	0.021	0.008	-

Table 4.4: The dipoles used in the reconstruction of intermediate sources and the respective NRMS errors.

The internal sources are chosen so that their distance from the sensor array is always approximately 8 mm. The external source was chosen randomly and normalized so that relative strength of sources  $D=1$ . The same external source was used for each reconstruction. The reconstruction results are demonstrated in Fig. 4.9.

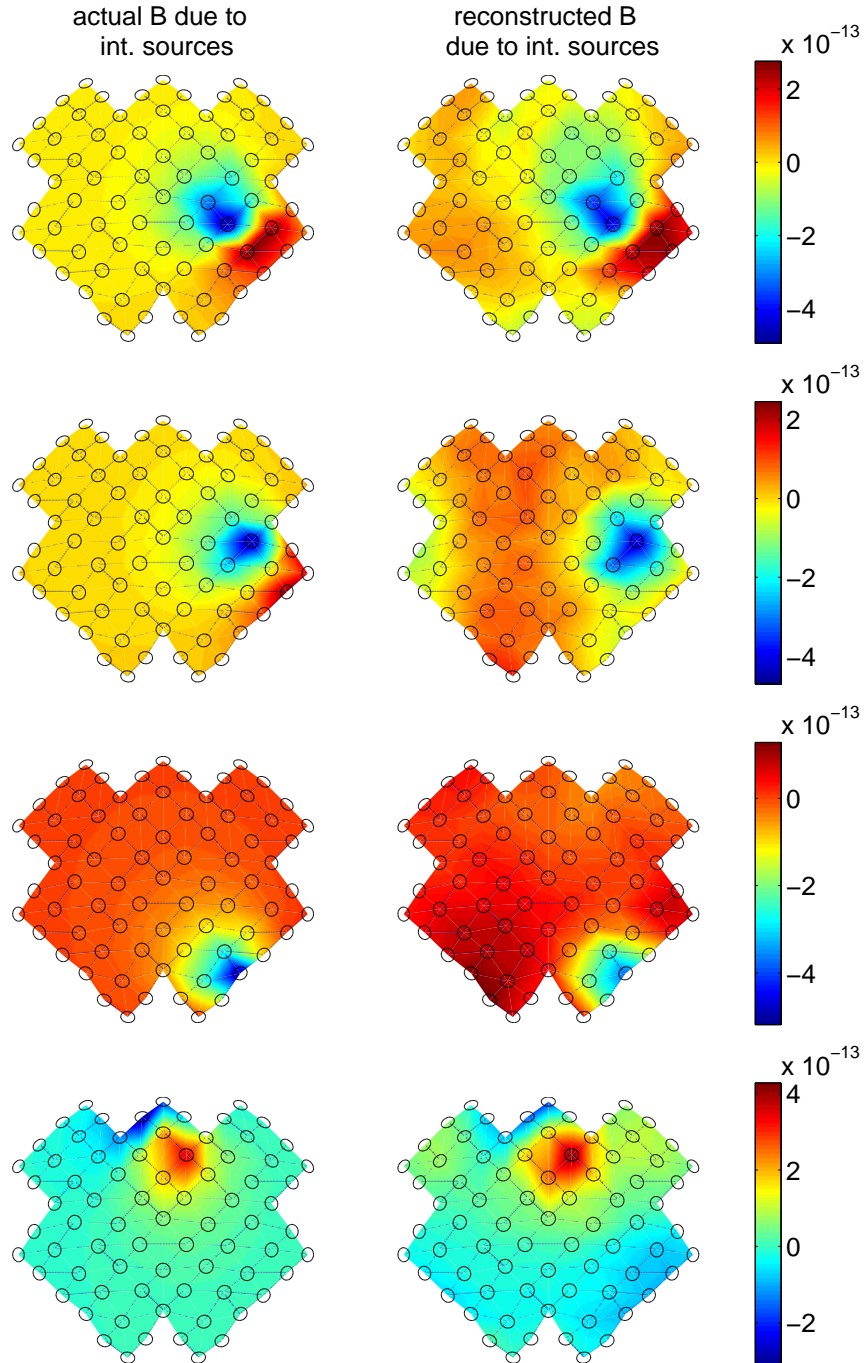


Figure 4.9: Reconstruction of the fields of four different intermediate sources. The sources are in the same order as in Table 4.4.

It is seen that the reconstruction quality diminishes gradually as the source is moved away from the center of the convergence sphere. This means that it is possible to get a picture of the source location even if it is not inside the convergence sphere. Then  $\mathbf{h}_0$  can be moved closer to the source, if a more accurate reconstruction is desired.

### 4.3.3 Filtering a time-dependent signal

So far in this work, SSS has been applied only to single points in time. To filter a time series, SSS is applied to each data point independently. To illustrate this, a current dipole with a sinusoidally time-dependent magnitude was placed about 5.6 m away from the sensor array. To simulate an evoked response, a current dipole was placed 1 cm away from the sensor array and given a time course resembling an evoked response of 100 ms duration. The results of the SSS filtering on one representative gradiometer channel are shown in Fig. 4.10.

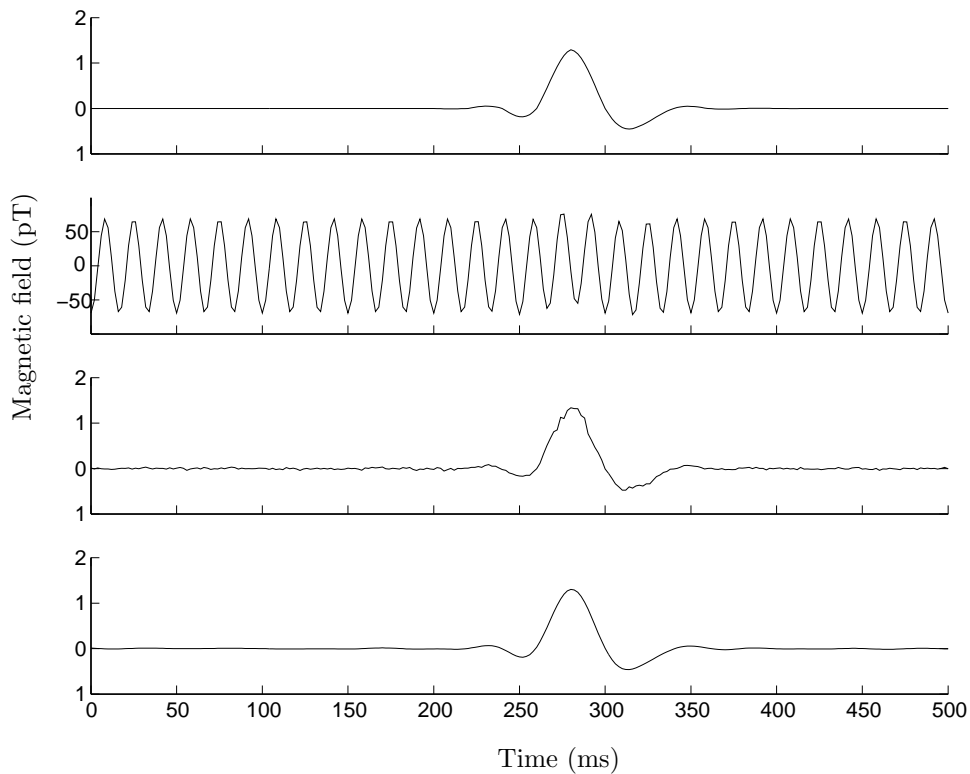


Figure 4.10: From top to down: the field produced by the simulated evoked response, evoked response masked by a 60 Hz disturbance, result of applying SSS to remove the disturbance, lowpass filtered SSS result.

SSS removes the 60 Hz disturbance. After removing the remaining simulated sensor noise from the SSS filtering result (using a 40 Hz lowpass filter), the original response is recovered. SSS does not distort the response.

## 4.4 Effect of nonideal properties of the sensor array

### 4.4.1 Errors in sensor geometry data

In a real world situation, there are errors in the gradiometer normal vector and location data used in the computation of the SSS matrix (Eq. 3.18) that will introduce an additional error into the reconstruction. To simulate this effect, the SSS matrix was computed using perturbed sensor data.

First, we studied the effect of a randomly directed rotation of each gradiometer by an angle chosen from a normal distribution ( $\mu = 0$ ). The standard deviation was varied from 0 to 3 degrees. The effect of this on the data of Fig. 4.7 (with  $D=1$ ) is shown in Fig. 4.11.

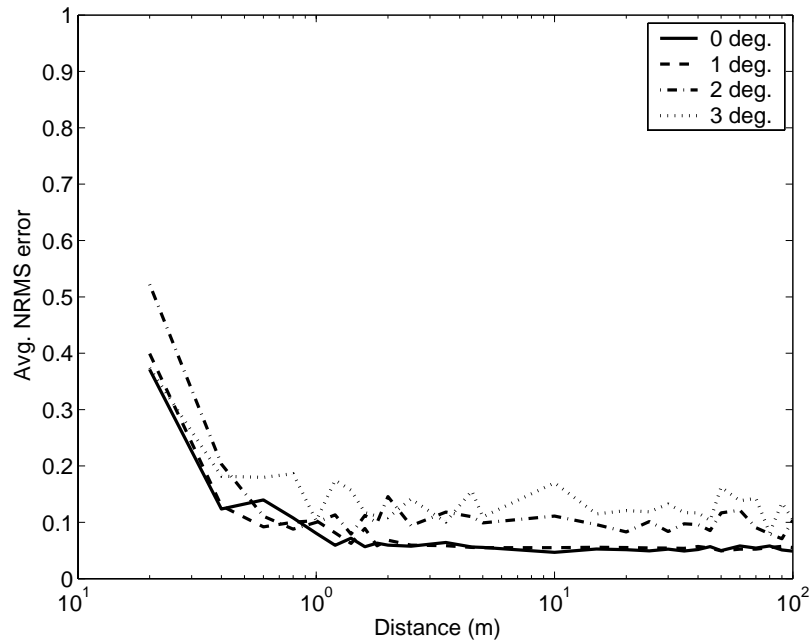


Figure 4.11: Effect of errors in the coil normal vectors.

It is seen that a standard deviation of 1 degree or less does not significantly

affect the reconstruction. At 2 degrees, the additional NRMS error is about 5 percentage points.

Next, the effect of errors in the coil coordinate data was studied in the same way. A small random error, chosen from a normal distribution with  $\mu = 0$  mm, was added to the  $x$ ,  $y$  and  $z$  coordinates of each gradiometer. The standard deviation of the distribution was varied from 0 to 2 mm.

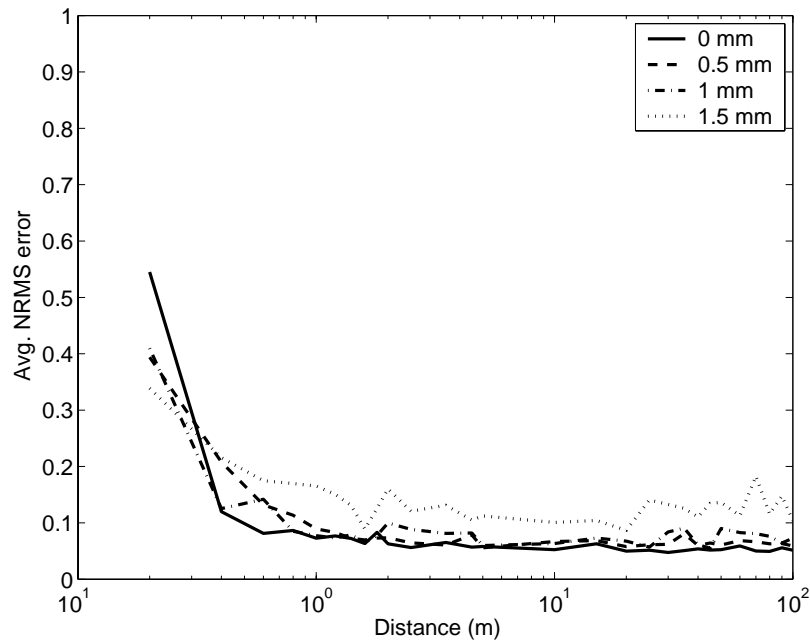


Figure 4.12: Effect of errors in the coil coordinates.

The result is similar to the normal vector rotations. The fact that small perturbations in the SSS matrices do not affect the reconstruction is due to the use of regularization. If the pseudoinverse solution was used, even small matrix perturbations would cause large errors in the solution.

#### 4.4.2 Gradiometer imbalance

Another source of error is imbalance of the gradiometers. Due to tolerances in manufacturing the instrument, the compensation coil does not have exactly the same ratio of measured field to applied field as the signal coil. For example, an imbalance of 0.1 % means that for the same applied field, the field values measured by the coils would deviate 0.1 % from each other.

The imbalance was simulated by multiplying the signal of each compensation

coil by a normally distributed random factor ( $\mu = 1$  and  $\sigma = f_i$ ) when computing the dipole fields, so that the standard deviation of the imbalance across sensors is  $f_i$ . The SSS matrix was then computed assuming zero imbalance. The data of Fig. 4.7 with  $D=1$  were recomputed for different values of  $f_i$ .

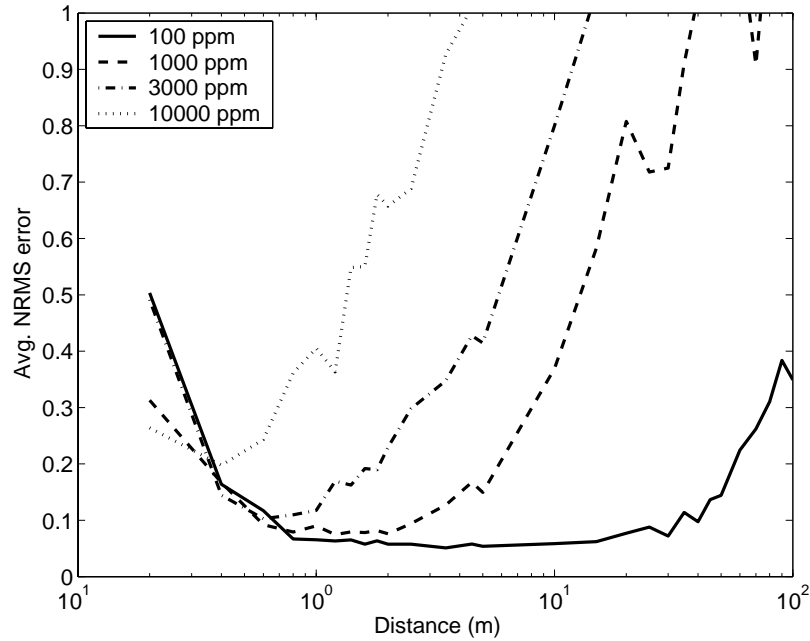


Figure 4.13: Effect of gradiometer imbalance.

The relative error caused by the imbalance is largest when the field values measured by the signal coil and the compensation coil are close to each other. Thus, the effect of the imbalance is seen first for distant sources, whose fields are spatially slowly varying near the sensor array. The SSS method is seen to be quite sensitive to imbalance, as the error is clearly visible at 100 ppm (0.01 %).

#### 4.4.3 Calibration errors

To compensate for the coil area and other factors, the voltage given by each SQUID is multiplied by a constant (Tesla per volt) to get the actual field value. There is a margin of error in determining these constants. To simulate the effect of calibration errors, the signal of each gradiometer was multiplied by a normally distributed random factor ( $\mu = 1$  and  $\sigma = f_c$ ) while computing the fields of the sources, while the SSS matrix was computed assuming no

calibration errors. Fig. 4.13 shows the result.

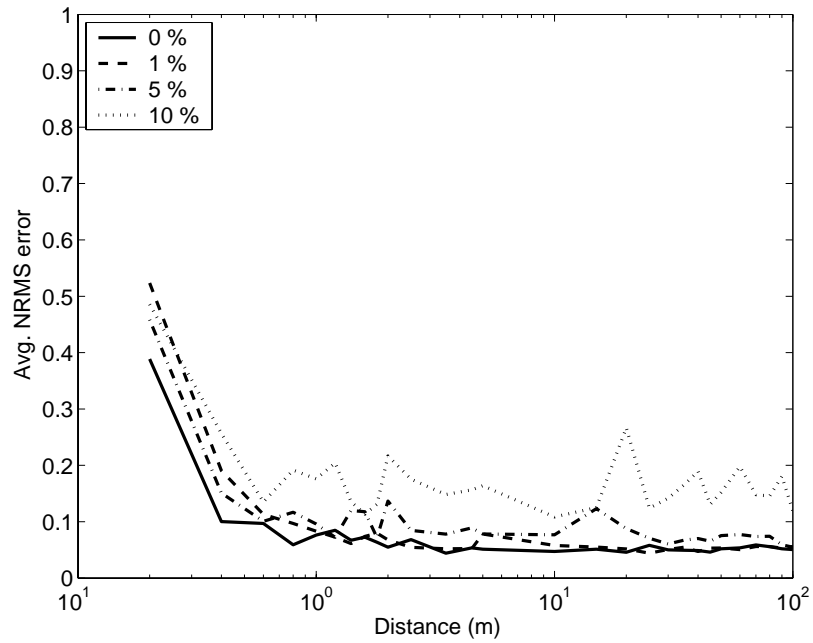


Figure 4.14: Effect of calibration errors.

It is seen that the calibration accuracy is not nearly as critical as imbalance. An accuracy of 1 % does not introduce any visible error, while 5 % still produces acceptable results.

## Chapter 5

# Discussion

It was found that applying the Signal Space Separation method to the babySQUID leads to the problem of inverting a severely ill-conditioned matrix. Essentially, this means that the basis vectors forming the SSS matrix are very similar, although the basis functions themselves are orthogonal. The problem does not arise in applying the SSS method to the Vectorview instrument used in [14], which has three different types of sensors (two types of planar gradiometers and magnetometers). It may be concluded that using different kinds of sensors gives a more complete characterization of the magnetic field and therefore a clearer difference between the basis vectors [13].

The PP-TSVD regularization method was found to be capable of dealing with the ill-conditioned SSS matrix. There is one regularization parameter that needs to be adjusted for the chosen SSS parameters. However, the optimal value of the parameter does not depend on the source configuration. This is important, as optimizing the parameter with respect to the source configuration would not be possible in a practical application of the method. A problem with the PP-TSVD regularization is that it is computationally quite expensive, making raw data processing consume few hours of time for each minute of data with typical sampling rates. Without regularization, solving the SSS problem would require just a single matrix multiplication, which would make it possible to apply the method in real time during data collection.

From the viewpoint of applying the SSS method, the second problem with the babySQUID is the relatively low number of sensors, which limits the number of basis vectors that can be used. The relatively small minimum source-sensor distance (about 8 mm) implies that the signal sources give rise to fields with high spatial frequencies and therefore increases the require-

ment for the number of basis vectors. For comparison, in the Vectorview instrument it can be assumed that all sources are at least 2 cm away from the sensors. The problem can be circumvented by using a small convergence sphere, but this limits the extent and location of the sources that can be reconstructed. If the dominant brain sources can be assumed to be confined into a certain known region (about 3–4 cm in radius), this will not be a problem. The number of basis vectors that can be used for the external (disturbance) sources is also limited, which is reflected in the NRMS vs. distance plots of Figs. 4.4–4.7. Apparently, there are not enough basis vectors to represent disturbance sources that are closer than about 1 m to the sensor array (depending on the SSS configuration). There are some disturbance sources that are typically quite close to the sensor array, such as the heart of the infant. However, at least in the case of the heart, it is relatively easy to remove the disturbance before applying SSS. In practice, the problem of limited channels is made worse by the fact that a few channels may be expected not to work during a typical measurement. This may make it necessary to use an SSS configuration with fewer basis vectors to get an overdetermined problem.

Assuming that the signal source is located within the internal convergence sphere and the disturbance source is far enough from the sensor array, the PP-TSVD regularized SSS is found to perform quite well with simulated data. For example, disturbance sources 5 m away that produce fields 10 times stronger than the signal source, therefore completely obscuring the signal, can be rejected and the signal source reconstructed with a NRMS accuracy of 10–20 %. This result is encouraging, but it is achieved under somewhat ideal conditions. Most importantly, the effects of nonideal properties of the MEG device are not taken into account.

The nonideal properties include discrepancies between the sensor location and orientation data and the real geometry of the sensor array, imbalance of the gradiometers, and calibration errors. Based on the simulations, it is expected that the inaccuracies of the geometry data and the calibration errors should not affect the reconstruction quality by more than 5–10 percentage points. However, based on the simulation experiment, an imbalance of 1 % or more seems to be too high for acceptable performance, while the imbalance of the wire wound babySQUID gradiometers is likely to be somewhere between 0.1 % and 1 %. With an imbalance of 0.1 % to 0.3 % usable results could still be produced, provided that there are no strong disturbance sources far away ( $> 10$  m) from the sensor array.

It should be noted that the sensor noise level of  $\sigma = 10$  fT used in the simulation is unrealistically low. Based on the true noise levels of the babySQUID, the real noise level is probably larger by a factor of 5 to 10, depending on

the bandwidth used. According to a few tests, it is expected that a noise level of  $\sigma = 100$  fT would uniformly worsen the NRMS values by about 10 percentage points, but would not change the results qualitatively.

For a final evaluation of the PP-TSVD regularized SSS, it should be tested by doing phantom measurements with the real instrument. The phantom is an artificial current source that produces a known magnetic field (e.g. a current loop) or a set of such sources. The magnetic field produced by a phantom in a noisy environment could be reconstructed with SSS and compared with the known theoretical field. Unfortunately, this kind of measurement could not be included in the work due to time constraints.

The work has some implications for design of future sensor arrays that utilize SSS. Perhaps the most important point is the benefit of having several types of sensors to better characterize the magnetic field and avoid ill-conditioning of the basis matrix. Another is the need to have a sufficient number of channels, since this determines the number of basis vectors that can be used. Finally, it is important to make sure that the gradiometers are balanced as well as possible.

## Conclusions

In this work, it was shown that the Signal Space Separation method can be successfully applied to simulated data on the babySQUID instrument. However, within numerical precision, the simulation results are computed assuming no imbalance, no calibration errors and no errors in the geometry data of the sensor array. From the simulations, it is clear that these factors will affect the real world performance significantly, though it cannot be said whether the method is rendered unusable or not. For that, tests on real data are needed.

The work was successful in that the problem of the severely ill-conditioned SSS matrix was solved and relevant information about the performance of the SSS method on the babySQUID was obtained. Also, the hardware requirements of the SSS method were clarified somewhat. An obvious shortcoming of the work is that it was not possible to study the performance of the method on real data. It is hoped that this can be done in future studies.

## Appendix A

# The Laplace equation and spherical harmonics

### A.1 Solving the Laplace equation

We denote spherical coordinates as  $(r, \theta, \phi)$ , where  $r$  is the radius from the origin,  $\theta$  is the polar angle measured from positive z-axis, and  $\phi$  is the azimuthal angle measured from positive x-axis. The corresponding unit vectors are denoted by  $(\mathbf{e}_r, \mathbf{e}_\theta, \mathbf{e}_\phi)$ . The Laplace equation  $\nabla^2 V = 0$  in spherical coordinates is

$$\frac{1}{r^2 \sin \theta} \left[ \sin \theta \frac{\partial}{\partial r} \left( r^2 \frac{\partial V}{\partial r} \right) + \frac{\partial}{\partial \theta} \left( \sin \theta \frac{\partial V}{\partial \theta} \right) + \frac{1}{\sin \theta} \frac{\partial^2 V}{\partial \phi^2} \right] = 0. \quad (\text{A.1})$$

We can solve this by separation of variables, using

$$V(r, \theta, \phi) = R(r)\Theta(\theta)\Phi(\phi). \quad (\text{A.2})$$

Substituting this into A.1 and multiplying by  $\sin \theta / (R\Theta\Phi)$  yields

$$\frac{\sin^2 \theta}{R} \frac{\partial}{\partial r} \left( r^2 \frac{\partial R}{\partial r} \right) + \frac{\sin \theta}{\Theta} \frac{\partial}{\partial \theta} \left( \sin \theta \frac{\partial \Theta}{\partial \theta} \right) + \frac{1}{\Phi} \frac{\partial^2 \Phi}{\partial \phi^2} = 0. \quad (\text{A.3})$$

Separating the  $\phi$ -dependent part first, we get

$$\frac{1}{\Phi} \frac{\partial^2 \Phi}{\partial \phi^2} = -m^2, \quad (\text{A.4})$$

where the separation constant  $-m^2$  is chosen in anticipation of a periodical dependency on the azimuthal coordinate  $\phi$ . This choice will make the solution easier, although it is not necessary. It is easily seen that the solution to Eq. A.4 is

$$\Phi(\phi) = e^{im\phi} \quad (\text{A.5})$$

and  $m$  is restricted to be an integer by the necessary condition  $\Phi(\phi + 2\pi) = \Phi(\phi)$ . Substituting the separation constant into Eq. A.3 and dividing by  $\sin^2 \theta$  yields another separated equation

$$\frac{1}{R} \frac{\partial}{\partial r} \left( r^2 \frac{\partial R}{\partial r} \right) = -\frac{1}{\Theta \sin \theta} \frac{\partial}{\partial \theta} \left( \sin \theta \frac{\partial \Theta}{\partial \theta} \right) + \frac{m^2}{\sin^2 \theta}. \quad (\text{A.6})$$

Using  $l(l+1)$  as a separation constant and multiplying by  $\Phi$ , we get first

$$\frac{1}{\sin \theta} \frac{\partial}{\partial \theta} \left( \sin \theta \frac{\partial \Theta}{\partial \theta} \right) + \frac{m^2}{\sin \theta} = l(l+1). \quad (\text{A.7})$$

Another multiplication by  $\Phi$  yields

$$\frac{1}{\Theta \sin \theta} \frac{\partial}{\partial \theta} \left( \sin \theta \frac{\partial \Theta}{\partial \theta} \right) + \Phi \left( l(l+1) - \frac{m^2}{\sin^2 \theta} \right) = 0. \quad (\text{A.8})$$

The reason for choosing the separation constant as  $l(l+1)$  is to obtain this form, which is the standard form of the associated Legendre equation. The solutions are the associated Legendre polynomials  $P_l^m(\cos \theta)$ , where  $l$  and  $m$  are integers,  $l \geq 0$  and  $|m| \leq l$ .

The remaining equation is then

$$\frac{1}{R} \frac{\partial}{\partial r} \left( r^2 \frac{\partial R}{\partial r} \right) = l(l+1). \quad (\text{A.9})$$

We try a solution  $R = r^k$ , which after substitution gives

$$k(k+1) = l(l+1). \quad (\text{A.10})$$

This quadratic equation in  $k$  is satisfied for  $k = l$  or  $k = -(l + 1)$ , giving the solutions  $R = r^l$  and  $R = 1/r^{l+1}$ . Finally, the complete solution with  $\alpha'_{lm}$  and  $\beta'_{lm}$  constants is

$$V = \sum_{l=0}^{\infty} \sum_{m=-l}^l \alpha'_{lm} \frac{1}{r^{l+1}} P_l^m(\cos \theta) e^{im\phi} + \sum_{l=0}^{\infty} \sum_{m=-l}^l \beta'_{lm} r^l P_l^m(\cos \theta) e^{im\phi}, \quad (\text{A.11})$$

which is usually written

$$V(\mathbf{r}) = \sum_{l=0}^{\infty} \sum_{m=-l}^l \alpha_{lm} \frac{Y_{lm}(\theta, \phi)}{r^{l+1}} + \sum_{l=0}^{\infty} \sum_{m=-l}^l \beta_{lm} r^l Y_{lm}(\theta, \phi) \quad (\text{A.12})$$

where the spherical harmonics  $Y_{lm}(\theta, \phi)$  are defined as

$$Y_{lm}(\theta, \phi) = \sqrt{\frac{(2l+1)(l-m)!}{4\pi(l+m)!}} P_l^m(\cos \theta) e^{im\phi}. \quad (\text{A.13})$$

The complex basic solutions (terms in Eq. A.12) are more convenient in calculations than the real solutions. However, we can obtain a real solution by replacing the azimuthal functions  $e^{im\phi}$  by  $\cos(im\phi)$  and  $\sin(im\phi)$  (which also satisfy Eq. A.4). One possible choice of the real spherical harmonics  $y_{lm}$  obtained in this way can be expressed as

$$y_{lm} = \begin{cases} \sqrt{2} \operatorname{Re}\{Y_{lm}\}, & m > 0 \\ Y_{lm} & , \quad m = 0 \\ \sqrt{2} \operatorname{Im}\{Y_{lm}\}, & m < 0 \end{cases} \quad (\text{A.14})$$

The  $\sqrt{2}$  is a normalization factor, which is not strictly necessary here but is used so that  $y_{lm}$  satisfy the same orthonormality properties as  $Y_{lm}$ . The solution in terms of the real harmonics is

$$V(\mathbf{r}) = \sum_{l=0}^{\infty} \sum_{m=-l}^l \alpha_{lm} \frac{y_{lm}(\theta, \phi)}{r^{l+1}} + \sum_{l=0}^{\infty} \sum_{m=-l}^l \beta_{lm} r^l y_{lm}(\theta, \phi). \quad (\text{A.15})$$

## A.2 Gradients of basic solutions

To calculate the magnetic field caused by each term, we need the gradients

$$\nabla \left( \frac{y_{lm}(\theta, \phi)}{r^{l+1}} \right) = \begin{cases} \sqrt{2} \operatorname{Re}\{\nabla \left( \frac{Y_{lm}(\theta, \phi)}{r^{l+1}} \right)\} & m > 0 \\ \sqrt{2} \nabla \left( \frac{Y_{lm}(\theta, \phi)}{r^{l+1}} \right) & m = 0 \\ \sqrt{2} \operatorname{Im}\{\nabla \left( \frac{Y_{lm}(\theta, \phi)}{r^{l+1}} \right)\} & m < 0 \end{cases} \quad (\text{A.16})$$

and

$$\nabla \left( r^l y_{lm}(\theta, \phi) \right) = \begin{cases} \sqrt{2} \operatorname{Re}\{\nabla (r^l Y_{lm}(\theta, \phi))\} & m > 0 \\ \sqrt{2} \nabla (r^l Y_{lm}(\theta, \phi)) & m = 0 \\ \sqrt{2} \operatorname{Im}\{\nabla (r^l Y_{lm}(\theta, \phi))\} & m < 0 \end{cases} \quad (\text{A.17})$$

Using the gradients of the complex functions involving  $Y_{lm}$  rather than explicitly computing the gradients of the real functions results in somewhat simpler expressions. The gradient in spherical coordinates operating on function  $f$  gives

$$\nabla f = \mathbf{e}_r \frac{\partial f}{\partial r} + \mathbf{e}_\theta \frac{1}{r} \frac{\partial f}{\partial \theta} + \mathbf{e}_\phi \frac{1}{r \sin \theta} \frac{\partial f}{\partial \phi}. \quad (\text{A.18})$$

By straightforward differentiation, we get

$$\begin{aligned} \nabla \left( \frac{Y_{lm}(\theta, \phi)}{r^{l+1}} \right) &= \mathbf{e}_r \frac{-l-1}{r^{l+2}} Y_{lm}(\theta, \phi) - \\ &\quad - \mathbf{e}_\theta \frac{1}{r^{l+2}} \sqrt{\frac{(2l+1)(l-m)!}{4\pi(l+m)!}} \sin \theta \left[ \frac{\partial}{\partial x} P_{lm}(x) \right]_{x=\cos \theta} e^{im\phi} + \\ &\quad + \mathbf{e}_\phi \frac{1}{r^{l+2}} \sin \theta im Y_{lm}(\theta, \phi) \end{aligned}$$

and

$$\begin{aligned} \nabla \left( r^l Y_{lm}(\theta, \phi) \right) &= \mathbf{e}_r l r^{l-1} Y_{lm}(\theta, \phi) - \\ &\quad - \mathbf{e}_\theta r^{l-1} \sqrt{\frac{(2l+1)(l-m)!}{4\pi(l+m)!}} \sin \theta \left[ \frac{\partial}{\partial x} P_{lm}(x) \right]_{x=\cos \theta} e^{im\phi} + \\ &\quad + \mathbf{e}_\phi r^{l-1} \sin \theta im Y_{lm}(\theta, \phi). \end{aligned}$$

The derivative  $\frac{\partial}{\partial x}P_{lm}(x)$  appearing in these equations is obtained in the next section.

### A.3 Associated Legendre polynomials

The associated Legendre polynomials arising in the solution of the Laplace equation are defined as

$$P_l^m(x) = (-1)^m(1-x^2)^{m/2} \frac{d^m}{dx^m} P_l(x), \quad l \geq 0, \quad |m| \leq l, \quad (\text{A.19})$$

where  $P_l$  is the Legendre polynomial, which plays a role in many mathematical and physical problems.  $P_l$  can be defined in different ways, one is Rodrigues' formula:

$$P_l(x) = \frac{1}{2^l l!} \frac{d^l}{dx^l} (x^2 - 1)^l. \quad (\text{A.20})$$

Despite the  $m$ -fold differentiation in Eq. A.19,  $P_l^m(x)$  will also be defined for negative  $m$ . This makes sense only after the definition of  $P_l$  is inserted into Eq. A.19, when we get

$$P_l^m(x) = (-1)^m(1-x^2)^{m/2} \frac{1}{2^l l!} \frac{d^{l+m}}{dx^{l+m}} (x^2 - 1)^l. \quad (\text{A.21})$$

Matlab includes a routine for computing numerical values of the associated Legendre polynomials, which is based on recurrence relations. For computing the derivative, we use the formula

$$\frac{d}{dx} P_l^m(x) = \frac{mx P_l^m(x) + (l+m)(l-m+1)\sqrt{1-x^2} P_l^{m-1}(x)}{1-x^2}, \quad (\text{A.22})$$

which is easy to obtain by differentiating Eq. A.21 and then using the recurrence relation [1]

$$P_l^{m+1}(x) + \frac{2mx}{\sqrt{1-x^2}} P_l^m(x) + (l+m)(l+m+1) P_l^{m-1}(x) = 0. \quad (\text{A.23})$$

Since Eq. A.22 involves  $P_l^{m-1}(x)$ , it cannot be used when  $m = -l$ . For that case, we can first use the relation [1]

$$P_l^{-m}(x) = (-1)^m \frac{(n-m)!}{(n+m)!} P_l^m(x) \quad (\text{A.24})$$

and compute the derivative for the positive  $m$  case.

# Bibliography

- [1] G. Arfken and H. J. Weber. *Mathematical Methods for Physicists*. Academic Press, San Diego, CA, 4th edition, 1995.
- [2] H. Berger. Über das elektroenkephalogram des menschen. *Archiv Psychiatrische Nervenkrankheit*, 87:527–570, 1929.
- [3] D. Cohen. Magnetoencephalography: Evidence of magnetic fields produced by alpha-rhythm currents. *Science*, 161:784–786, 1968.
- [4] D. Cohen. Detection of brain’s electric activity with superconducting magnetometer. *Science*, 175:664–666, 1972.
- [5] R. Cools. An encyclopedia of cubature formulas. *Journal of Complexity*, 19:445–453, 2003.
- [6] M. Hämäläinen, R. Hari, R. J. Ilmoniemi, J. Knuutila, and O. V. Lounasmaa. Magnetoencephalography - theory, instrumentation and applications to noninvasive studies of the working human brain. *Reviews of Modern Physics*, 65(2):413–497, 1993.
- [7] P. C. Hansen. Matlab implementation of PP-TSVD regularization. <http://www.imm.dtu.dk/~pch/Regutools/pptsvd.m>.
- [8] P. C. Hansen. Regularization Tools: A Matlab package for analysis and solution of discrete ill-posed problems. *Numerical Algorithms*, 6:1–35, 1994.
- [9] P. C. Hansen and K. Mosegaard. Piecewise polynomial solutions without a priori break points. *Numerical Linear Algebra with Applications*, 3:513–524, 1996.
- [10] Y. Okada, C. Atwood, K. Pratt, and D. Paulson. babySQUID: a high-resolution, mobile, multichannel MEG system for neonatal brain assessment. *Proceedings of Biomag 2004*, page 660.

- 
- [11] J. Sarvas. Basic mathematical and electromagnetic concepts of the biomagnetic inverse problem. *Physics in Medicine and Biology*, 32:11–22, 1987.
  - [12] A. H. Stroud. *Approximate Calculation of Multiple Integrals*. Prentice-Hall, Eaglewood Cliffs, NJ, 1971.
  - [13] S. Taulu. Private discussion.
  - [14] S. Taulu, M. Kajola, and J. Simola. Suppression of interference and artifacts by the signal space separation method. *Brain Topography*, 16(4):269–275, 2004.